Polymorphs of ZnV_2O_6 Under Pressure: a First Principle Investigation

Armando Beltrán, Lourdes Gracia[$] and Juan Andrés[*]*

Departament de Química Física i Analítica, Universitat Jaume I, Campus del Riu Sec, E-12071 Castelló de la Plana, Spain,

[$]Permanent address: Departament de Química Física, Universitat de València (UV), E-46100 Burjassot, Spain

ABSTRACT

This work presents first-principle calculations on the pressure-dependence of the stabilities, structures, and electronic properties of several polymorphs of ZnV_2O_6 under the pressure range 0-30 GPa. These properties are analyzed and discussed in detail using the different parameterizations of the exchange-correlation functional (B3LYP, HSE06, and PBE), and the results are compared with available experimental data. An extensive search process was carried out on the potential energy surface for a set of twelve possible polymorphs. Ten of them are stationary points, but only five have positive frequency values in the range of 0-30 GPa, i.e., monoclinic brannerite (*C*2/*m* and *C*2), orthorhombic columbite (*Pbcn*), trigonal $CaAs_2O_6$-type (*P*321), and triclinic NiV_2O_6-type ($P\bar{1}$). The monoclinic $ThTi_2O_6$-type (*C*2/*c*) phase presents a very low imaginary frequency around 50 cm^{-1}. Orthorhombic SrV_2O_6-type and BaV_2O_6-type, tetragonal trirutile and trigonal $PbSb_2O_6$ -type structures show several imaginary negative frequencies between -400 and -100 cm^{-1}. These imaginary frequencies are indicative of structural instabilities. All attempts to try to converge the calculations to obtain the $MoLa_2O_6$-type and HgV_2O_6-type polymorphs, by using the three functionals, have been unsuccessful. For both brannerite,$ThTi_2O_6$-type, columbite, $CaAs_2O_6$-type, NiV_2O_6-type structures numerical and analytical fittings were performed to obtain the lattice parameters, the bulk modulus, *B*, and their pressure derivative, *B*′, and the energy-volume relationship of phases are analyzed. Vibrational calculations were performed at each pressure for each polymorph and compared with available experimental data.

This study reports, for the first time, a complex and unexpected structural and chemical behavior as a function of pressure. An analysis of the results shows that brannerite monoclinic polymorphs present similar energies, suggesting that both structures may coexist in the range of pressures that were studied. Theoretical prediction reveals that, as the pressure increases, the most stable polymorph of ZnV_2O_6 moves from the monoclinic phase, *C*2/*m* (and *C*2), to the orthorhombic

columbite structure (*Pbcn)* and the corresponding transition pressure is computed to be 5 GPa at the B3LYP level; however, using the HSE06 and PBE functionals, the $FeNb_2O_6$-type structure is the most stable polymorph from ambient pressure up to 30 GPa. In addition the calculations show that the $ThTi_2O_6$-type phase (*C*2/*c*) becomes more stable than the other two monoclinic structures above 15, 13, and 8 GPa using the B3LYP, HSE06, and PBE functionals, respectively. The findings reported here indicate that the method used to predict relative phase stabilities and phase transitions should be chosen carefully, and that the results should be scrutinized with a critical eye. We analyze the variations of different vibrational frequencies and V−O and Zn−O bond lengths as pressure is applied, and the results confirm that Badger's lineal relationships were not found for the monoclinic polymorphs (*C*2/*m*, *C*2, and *C*2/*c*) due to the presence of a charge transfer process from the ZnO_6 to the VO_6 polyhedra. In addition, we determined the stability of ZnV_2O_6 against binary oxides (VO_2, V_2O_5, and ZnO), or metals (Zn and V) and oxygen, and the results reveal that the decomposition channels are not energetically feasible. The present work provides a new perspective on the variations of crystal structures and physical properties at high pressure in ZnV_2O_6 polymorphs. With the wealth of data presented, this study aims to encourage further basic and experimental research on an interesting case of ZnV_2O_6-based materials with novel properties that may be the basis of important innovations for industrial applications.

1 Introduction

The response of materials to pressure is a growing scientific domain, especially in condensed-matter physics, crystal chemistry, geophysics, biology, and materials science, for the analysis of new phenomena[1-4] and it is an attractive area for fundamental theory and simulations.[3,5-15] By applying pressure, the physical and chemical properties of condensed matter can be significantly altered due to the fact that the atoms approach each other by modifying the interatomic distances with concomitant changes in the local environment and bonding patterns, which may lead to the formation of new structures (polymorphs) through phase transitions.[16-18] Therefore, high pressure can continuously modulate crystal and electronic structures, revealing the underlying transformation mechanism and giving rise to new materials with unexpected physical and chemical properties that are not accessible under ambient conditions.[19-21] Knowledge of how these basic interactions within the system evolve under extreme conditions is fundamental to help understand their technological applications.

High pressure experiments on materials, such as static pressure using a diamond anvil cell[22] and dynamic pressure using shock waves,[23] are of considerable interest from both a basic and an applied point of view. However, high pressure is not easy to achieve/access and control in X-ray diffraction experiments using these techniques. In this context, using and applying reliable theoretical methods which simulate such properties would help significantly. Atomic-level information is the key to the exploration of the properties of materials. The utilization and application of reliable theoretical methods and computational models which simulate such properties would be a valuable aid, in particular by performing first-principles calculations, mainly within the framework of density functional theory (DFT).[16,24] In this context our group is engaged in a large research project devoted to finding crystal structures under pressure on different complex metal oxides such as Zn_2SnO_4,[25] $CaSO_4$,[26] Ag_2MoO_4,[27] and $AgVO_3$.[28]

The existence of at least two different crystal structures of the same compound, known as polymorphism, is well known.[29] Metavanadate MeV_2O_6 (Me = divalent metal ions) compounds at normal pressures have the brannerite structure and a rich variety of possible polymorphs that are dependent on pressure and temperature, i.e., orthorhombic columbite (*Pbcn*),[30] tetragonal trirutile ($P4_2/mmm$) and trigonal $PbSb_2O_6$ ($P\bar{3}1m$) structures have been reported.[31] Beck[32] developed the coordination number rule and the rule of hardness to rationalize inorganic coordination structures and the available structures for the compounds with AB_2O_6 stoichiometry, as occurs in ZnV_2O_6, and this author proposes the following polymorphs: $CaAs_2O_6$ (*P*321),[33] $FeNb_2O_6$ (*Pbcn*),[34] CaV_2O_6 (*C2/m*),[35]

SrV_2O_6 (*Pnma*),[36] BaV_2O_6 (*C*222),[37] HgV_2O_6 (*Pbca*)[38] NiV_2O_6, ($P\bar{1}$),[39] $MoLa_2O_6$ ($I\bar{4}2m$),[40] $ThTi_2O_6$ (*C2/c*),[41] and $ThTi_2O_6$ (*C2/m*).[42]

ZnV_2O_6 is a representative member of the AB_2O_6 family[31] and has been studied intensively due to its technological importance, and very recently Butt et al.[43] and Sun et al.[16] reported large-scale synthesis of ZnV_2O_6 nanostructures, highlighting its potential as a material for energy storage/conversion. Their monoclinic brannerite-type structure had been refined in space group *C*2 by earlier work, but subsequent studies showed that a reasonable description of the "average" structure should be achieved in the centrosymmetric space group *C*2/*m*.[44] More recently, Tang et al.[45] concluded that subtle changes induced by an external pressure are capable of causing a reversible structural phase transition at ZnV_2O_6 between the brannerite *C*2 and *C2/m* polymorphs.

The lack of systematic investigations on the solid state chemistry, energetic stability, and corresponding properties for all the available polymorphs of ZnV_2O_6 greatly precludes a full understanding of the structural determination and their corresponding physical and chemical properties. Thus, the unusual transition behaviors in the corresponding polymorphs with unusual properties drew our attention and led us to investigate their unopened transformation phases over a broad pressure range, with the aim of exploring their novel characteristics.

Herein, we report on the first extensive quantum-chemical calculations on the geometry, electronic structure, and relative stability of all available polymorphs of ZnV_2O_6 in a range of pressure from 0 to 30 GPa. These compounds are theoretically characterized by calculating the geometry and the electronic and vibrational properties using first principles DFT. The influence of different parameterizations of the exchange-correlation functional (B3LYP, HSE06, and PBE) on the properties investigated is discussed in detail, and the results are compared with available experimental data. The different bond compressibility and the possible phase transformations, explored by analyzing the respective equations of state (EOS) and obtaining the corresponding bulk modulus and transition pressures, are studied. The characterization the electronic structures, including the density of states (DOS) and band structures have been calculated, and we also perform an analysis of the energetic stability of the decomposition channels toward the corresponding metals and oxygen and binary metal oxides. Such a systematic approach is especially important for ZnV_2O_6 because the energetic separation and the structural differences between the various polymorphs are small and therefore potentially sensitive to details of the computational procedure. The results obtained here can enrich the structural properties of ZnV_2O_6 based materials but also are beneficial to provide an important reference for their application in practice. We believe that our study can further stimulate experimental and theoretical efforts on ZnV_2O_6 polymorphs.

The paper is organized as follows. Section 2 describes the computational details. Our results are discussed in four separate subsections within section 3: structural, energetic, vibrational, and electronic properties. The main conclusions are summarized in the last section, section 4.

2 Computational details

First-principles total-energy calculations were carried out within the periodic DFT framework using the CRYSTAL14 program package [46]. The density functional approximations applied were the popular B3LYP [4748] and HSE06 [49] hybrid functionals, as well as the widely used PBE functional.[50] Zn, V, and O centers have been described by 86-4111d41G, 86-411d3G, and 6-31d1G all electron basis sets, respectively, which are available at the CRYSTAL basis-set site.[51]

The diagonalization of the Fock matrix was performed on adequate *k*-point grids in the reciprocal space, which depend on the phase under treatment, using Pack–Monkhorst/Gilat shrinking factors (IS=ISP=4), the total number of k-points being 24, 24, 68, 27, 64, 64, 52, 30, 40, 34, 34, and 112 for the *C*2/*m*, *C*2, *C*2/*c*, *Pbcn*, *Pnma*, *Pbca*, *C*222, $I\bar{4}2m$, $P4_2/mmm$, *P*321, $P\bar{3}1m$, and $P\bar{1}$ ZnV_2O_6 structures, respectively. In addition, 27, 12, 8, and 12 k-points were used for the V_2O_5 (*Pmmn*), ZnO ($P6_3mc$), V (*Im*3*m*), and Zn ($P6_3/mmc$) phases, respectively. The use of a different number of k-points is because of the different symmetry of the corresponding unit cells. Thresholds controlling the accuracy of the calculation of Coulomb and exchange integrals were set to 10^{-8} (ITOL1 to ITOL4) and 10^{-14} (ITOL5), which ensure a convergence in total energy better than 10^{-7} hartree in all cases, whereas the percentage of Fock/Kohn-Sham matrices mixing was set to 40 (IPMIX = 40).[46]

In order to take into account van der Waals interactions, which can in fact play a significant role in this type of systems, the semiempirical Grimme extension of the standard DFT method (DFT+D) is an effective way of incorporating dispersion interactions, and it has proven its ability to provide reliable modeling of geometries and a better description of this type of interaction in metal oxides. Therefore, the empirical correction scheme to energy that considers the long-range dispersion contributions proposed by Grimme[52] and implemented by Bucko et al.[53] for periodic systems was used. The basic strategy in the development is to restrict the density functional description to shorter electron correlation lengths scales and to describe situations with medium to large interatomic distances by damped $C_6^{ij} \cdot R_{ij}^{-6}$ terms, where C_6^{ij} denotes the dispersion coefficient for atom pair *ij*, and R_{ij} is the corresponding interatomic distance.[52]

The choice of the exchange–correlation functional is of critical importance here as it has a significant influence on the properties obtained. (C. Freysoldt, B. Grabowski, T. Hickel, J. Neugebauer, G. Kresse, A. Janotti and C. G. van de Walle, Rev. Mod. Phys., 2014, 86, 253). To study

the influence of different approximations for exchange and correlation on the DFT results for ZnV_2O_6, we performed a complete structure optimization by using the B3LYP, HSE06, and PBE functionals. The electronic structures, including the DOS and band structures, were calculated based on the optimized geometries. The vibrational frequencies calculation in CRYSTAL was performed at the Γ point within the harmonic approximation, and the dynamic matrix was computed by the numerical evaluation of the first derivative of analytical atomic gradients. The Raman intensities were obtained by a coupled-perturbed Hartree-Fock/Kohn-Sham approach calculation under Placzeck approximation[54] and their values were normalized to the most intense peak.

In this work, we characterized the mechanical properties of the structures considered by investigating their bulk moduli. The bulk modulus describes the ability of an object to change its volume under the influence of uniform hydrostatic compression. The optimization followed a Quasi-Newton scheme. Gradients were evaluated every time the total energy was computed and the second derivative matrix (i.e., Hessian matrix) was built from the gradients. The default choice for the initial Hessian matrix was obtained from a Hessian model, as proposed by Schlegel and updated by using the Broyden-Fletcher-Goldfarb-Shanno algorithm.[55-59] All the structures were fully relaxed at the different pressures whenever possible (from 0 to 30 GPa) to their equilibrium configuration through the calculation of the forces on atoms and the stress tensor. In the relaxed configurations, the forces on the atoms were less than 0.0001 hartree/bohr = 0.005 eV/Å, and deviations of the stress tensor from a diagonal hydrostatic form were less than 0.1 GPa. An explicit estimation of the Pulay forces are not available for the time being in the CRYSTAL14 version, yet we are confident about our results because the Pulay stress is partly neglected when using a relatively large basis set, such as in the present work, as stated in other studies.[60] The mechanical stability for the $ThTi_2O_6$-type phase (*C*2/*c*) was analyzed by calculating the corresponding symmetrized elastic constant at several pressures. From these elastic constants we applied the Born criteria[61] for the confirmation of the stable structure.

The CRYSTAL program can perform an automated scan over the volume to compute energy E vs. volume V curves that are then fitted to the third-order Birch-Murnaghan (BM) EOS.[62] For each volume, a full V-constrained geometry optimization was performed. As a result, the pressure dependence of the atomic and electronic structure was determined, such as zero pressure bulk modulus, B_0, and its pressure derivative, B_0', values as well as the volume/pressure dependence of the total energy and enthalpy. Following this procedure, enthalpy−pressure curves were obtained for the three ZnV_2O_6 polymorphs and the corresponding values of pressure for induced phase transitions were calculated.

To consider the effect of pressure on the vibrational-frequencies of this system, we optimized geometrical parameters and internal positions of all phases, at a number of fixed external pressures. Three types of decomposition channels were studied and the corresponding decomposition enthalpy, $\Delta_d H^0$, at ambient temperature was calculated using the following equations:

(i) Formation of metal oxides

$$\Delta_d H^0 = \sum_{\mathrm{i}}^{metal\ oxides} H_{\mathrm{i}}^0 - H_{ZnV_2O_6}^0$$

(ii) Formation of metal oxides, metals, and oxygen

$$\Delta_d H^0 = \sum_{\mathrm{i}}^{metals\ +\ metal\ oxides} H_{\mathrm{i}}^0 + H_{O_2}^0 - H_{ZnV_2O_6}^0$$

(iii) Formation of metals and oxygen

$$\Delta_d H^0 = \sum_{\mathrm{i}}^{metals} H_{\mathrm{i}}^0 + H_{O_2}^0 - H_{ZnV_2O_6}^0$$

where $H_i^0 = (E_{EL} + E_0 + pV)$. Here, E_{EL} is the total electronic energy, E_0 is the zero point energy, and for both metal oxides and single metals the most stable solid polymorphs at ambient pressure and temperature were considered in our calculations. The equilibrium structures were obtained by optimizing all the geometric parameters.

To minimize errors due to incorrect estimation of the O_2 binding energy, which was significantly overestimated by 1-1.5 eV when the standard DFT functionals were used,[63-65] we employed a water reference instead of a molecular oxygen-based reference,[66] following the equation: $\frac{1}{2}H_{O_2}^0 = H_{H_2O}^0 - H_{H_2}^0$.

3 Results and discussion

3.1 Searching ZnV_2O_6 polymorphs

First, we performed an intensive search process for the characterization and analysis of the possible polymorphs of ZnV_2O_6, some of which were found experimentally while others have been proposed in the bibliography.[16,30-32,43-45] The following twelve polymorphs were studied at the B3LYP, HSE06, and PBE computational levels: orthorhombic (*C*222, *Pbcn*, *Pnma*, *Pbca*), monoclinic (*C*2, *C*2/*m*, and *C*2/*c*), trigonal ($P\bar{3}1m$ and *P*321), tetragonal ($I\bar{4}2m$ and $P4_2/mmm$), and triclinic ($P\bar{1}$). The results can be summarized as follows: the *C*2, *C*2/*m*, *Pbcn*, *P*321, $P\bar{1}$, C2/*c*, *Pnma*, *C*222, $P4_2/mmm$ and $P\bar{3}1m$ were localized and characterized as stationary points in the potential energy surface (PES), whose first derivative of the energy with respect to the nuclear coordinates was zero, while the second

derivatives of the energy (which are proportional to the square root of the vibrational frequency) presented positive (real) values for the *C*2, *C*2/*m*, *Pbcn*, *P*321, and $P\bar{1}$ polymorphs and they were minima in the range of pressures that were studied: 0-30 GPa. The *C*2/*c* polymorph displays one imaginary frequency around a very low value of about -50 cm^{-1}, with the three functionals. The *Pnma*, *C*222, $P4_2/mmm$, and $P\bar{3}1m$ polymorphs presented several imaginary frequencies in the range of -400 to -100 cm^{-1}, except *Pnma*, which did not converge with any of the three functionals at pressures in the range 15-30 GPa. These imaginary frequencies associated to negative curvatures of the PES are indicative of structural instabilities. Any attempt to try to converge the calculations to obtain the $\boldsymbol{I\bar{4}2m}$ and *Pbca* polymorphs, by using the three functionals, has been unsuccessful. These results will be analyzed and discussed in detail in the next subsections.

3.2 Structural properties

Calculated parameters of the monoclinic *C*2/*m*, *C*2 and *C*2/*c*, orthorhombic *Pbcn*, trigonal *P*321, and triclinic $P\bar{1}$ structures together with the available experimental data are reported in Table 1, while polyhedral representations of these six structures are depicted in Figure 1. In addition, atomic positions for these structures are collected in the supporting information (Table S1). For the *Pnma*, *C*222, $P4_2/mmm$, and $P\bar{3}1m$ polymorphs, the corresponding geometrical parameters and polyhedral representations are shown in the supporting information (Table S2 and Figure S1).

Insert Table 1 and Figure 1

For the sake of simplicity, the results of the B3LYP calculations are discussed first, and when discrepancies with respect to the results obtained with the other two functionals are detected, the corresponding differences will be commented on. In the monoclinic *C*2/*m* structure (Figure 1a) the Zn ions are octahedrally coordinated forming ZnO_6 clusters and the V cations have an irregular six-fold coordination, VO_6, while the O ions form a distorted cubic close-packed network. The distorted ZnO_6 clusters present two types of O anions, O1 and O2, with different values of the *Zn-O* distances, while the distorted VO_6 present five different values of *V-O*: *V-O1*, where O1 are coordinated to both Zn and V cations, O1´, two identical V-O2´, O3´ and O4´ (see Table 2). The ZnO_6 octahedra linked by their edges form anionic rows along the b axis, and the VO_6 octahedra joined by opposite vertices form chains also running parallel to the [010] direction and link the anionic layers.

Insert Table 2

A comparison of the reported values of monoclinic *C*2 and *C*2/*m* polymorphs shows that the both structures present similar geometries, and C2 is just a distortion from C2/m. (see Figure 1a and 1b,

and Table 2). The monoclinic *C*2/*c* structure (Figure 1c) presents layers of distorted VO_6 octahedra in the (011) plane joined by distorted ZnO_6 octahedra along the [100] direction. There are three different *Zn-O* distances: Zn-O1, Zn-O2 and Zn-O3, while the distorted VO_6 octahedra present five different *V-O* distances (see Figure 1c and Table 2). The oxygen anions O1 and O3 belong to the local coordination of both Zn and V cations (see Figure 1c). In the orthorhombic structure *Pbcn* (Figure 1d and Table 2) the ZnO_6 octahedra, linked by the edges, form anionic rows along the [011] direction, whereas the VO_6 are also linked by the edges and are parallel to the [011] direction. ZnO_6 clusters are distorted with three different *Zn-O* distances (Zn-O1, Zn-O2 and Zn-O3), while VO_6 octahedra present six different *V-O* distances. The O1 and O3 anions are located at the common vertex shared by both distorted ZnO_6 and VO_6 octahedra (see Figure 1d).

The trigonal *P*321 polymorph (Figure 1e) is composed of alternate parallel layers of ZnO_6 and VO_6 triangular prisms, the ZnO_6 being linked by the vertices with an array of triangular VO_6 prisms joined to each other by the edges running parallel to the [001] direction. There are six equal *Zn-O1* distances, and two different *V-O* distances (V-O1 and V-O1'). The O1 and O1' anions share both ZnO_6 and VO_6 triangular prisms. In the triclinic $P\bar{1}$ structure (Figure 1f) there are two different ZnO_6 octahedra linked by the edges forming rows along the c axis, joined to one another by chains of VO_6 and VO_4 polyhedra also running parallel to the [001] direction.

By fitting our theoretical B3LYP results to a third-order BM EOS for the *C*2/*m* phase, the following values have been calculated: bulk modulus: B_0 = 146.74 GPa, and B_0' = 5.11, to be compared with those obtained from experimental data [45] B_0 =147 GPa and B_0' fixed to 4. It is important to remark that we find that the cell parameters are overestimated (a= 9.296 Å, b=3.592 Å, c= 6.579 Å, and β =112.87º) and Grimme's correction is needed to obtain values (a=9.242 Å, b=3.528 Å, c= 6.573 Å, and β =111.13º) in better agreement with the reported experimental data (see Table 1 (a)).

For the *C*2/*m* polymorph, the values of the optimized lattice parameters differ from the experimental values[44] by less than 0.25%, 1.08%, and 2.28%, at the B3LYP, PBE, and HSE06 levels, respectively. Table 1 (b) displays the calculated structural parameters of the *C*2 phase (a= 9.240 Å, b=3.529 Å, c= 6.574 Å, and β =111.05º at the B3LYP level), which are very similar to those obtained for the *C*2/*m* phase and are also in good agreement with the experimental data. We obtain a bulk modulus B_0 = 137.25 GPa, and B_0' = 6.24 for the *C*2 polymorph. The results presented in Table 1 (d) show that the calculated values of the structural parameters for the orthorhombic *Pbcn* phase also agree well with the experimental values, 0.48%, 0.73%, and 1.81% at the PBE, B3LYP, and HSE06 levels, respectively, and an analysis of the optimized calculated parameters shows that the results obtained at the B3LYP and PBE levels are very close (see Table 1 (c, e, f)), the compressibility of the *P*321 and

*C*2/*c* polymorphs being similar to that of the *C*2/*m* phase, whereas the $P\bar{1}$ phase is slightly more compressible.

The *Pbcn*, *P*321, *C*2/*m*, *C*2, *C*2/*c* and $P\bar{1}$ polymorphs have been optimized at different pressures, and the calculated B3LYP values of interatomic distances are listed in Table 2. An analysis of the results reveals that similar values of both *C*2/*m* and *C*2 monoclinic space groups can be sensed. In the *C*2/*m*, *C*2, and *C*2/*c* monoclinic structures, the V cations show a 5 + 1 coordination with the six nearest oxygen ions, whereas the Zn cations always present a less distorted octahedral coordination, both ZnO_6 and VO_6 polyhedra being slightly more distorted in the *C*2 and *C*2/*c* phases.

In the case of the orthorhombic *Pbcn*, we also find a 5 + 1 local coordination around the V cations and the values of the *V-O* distances are in the range 1.663–2.223 Å, while in the *C*2/*m*, *C*2, and *C*2/*c* phases, the corresponding values are in the range of 1.662–2.447 Å, 1.662–2.446 Å and 1.702–2.172 Å, respectively. The ZnO_6 octahedra of the *Pbcn* phase are slightly more distorted than those of the monoclinic structures. The trigonal *P*321 phase presents an ordered six-fold coordination around the Zn cations with a Zn-O distance of 2.143 Å at ambient pressure and a 3 + 3 local coordination around the V cations with two different *V-O* distances of 1.721 and 2.100 Å, respectively. The triclinic $P\bar{1}$ structure presents three different types of polyhedra around the V cations, two of them with 5 + 1 coordination (noted as VO_6-1 and VO_6-2 in Figure 1f) with the values of the *V - O* distances in the range of 1.608–2.353 and 1.616–2.315 Å, respectively, and one VO_4 distorted tetrahedra with four different *V-O* distances between 1.666 and 1.779 Å. There are also two different ZnO_6 polyhedra, one of them with 3 different *Zn1-O* distances between 2.031 and 2.052 Å, and the other with 6 different *Zn2-O* distances in the range of 2.015–2.167 Å.

The axial compressibility of different polymorphs has been explored being the variation of the cell parameters with the pressure is not isotropic. As we can see in Table 2 the values of the *V-O* and *Zn-O* distances decrease monotonically as a function of pressure. We calculated the bond compressibility, χ, defined as: $-\frac{1}{d((Zn/V)O)}\frac{\partial\, d((Zn/V)O)}{\partial P}$, where *d*((*Zn/V*)*O*) are the (Zn/V)-oxygen distances from the values in Table 2. As expected, the compressibility of the longest *V-O4'* distance is higher for the *C*2/*m* (and *C*2) monoclinic phase than that of the short *V-O*(*1-3'*) distances. In the case of the *C*2/*c* monoclinic phase the compressibility of the largest *V-O4'* bond is also higher than the other short *V-O*(*1-3'*) bonds but with a lower value with respect to the other two monoclinic structures, *C*2/*m* and *C*2, the VO_6 octahedra being less distorted in this case. For *C*2/*m* (and *C*2) *Zn-O* the bonds are also less compressible than the *V-O4'* bond but more compressible than the rest of the *V-O*(*1-3'*) bonds.

For the *Pbcn* polymorph, the *V-O5'* bond is more compressible than the other *V-O*(*1-4'*) bonds, while the *Zn-O3* distance is the most compressible, followed by the *V-O5'* distance (see Table 2 and Figure 1d). At the *P321* polymorph, the *Zn-O* bonds present a higher compressibility than the *V-O* ones. In the $P\bar{1}$ structure, the *Zn2-O6* bond of the more distorted ZnO_6-2 octahedra is the most compressible followed by the long *V(1,2)-O8* bonds of both VO_6-1 and VO_6-2 octahedra.

In Table 2 we present the pressure variation of the Jahn Teller (JT) distortion parameter, σ_{JT}, defined as:[67] $\sigma_{JT}(Zn/V) = \sqrt{\sum_{i=1}^{6}\left(d((Zn/V)O)_i - d(\overline{(Zn/V)O})\right)^2}$ (where $d((Zn/V)O)_i$ are the six metal-oxygen distances of the (Zn/V)O_6 octahedra and $d(\overline{(Zn/V)O})$ is the average *(Zn/V)O* distance). From the optimized distances we found that the σ_{JT} for the VO_6 octahedra in both the *C*2/*m* and the *C*2 monoclinic phases are reduced from 0.667 Å at ambient pressure to 0.467 Å at 30 GPa. Hence, compression induces a 30% decrease in the VO_6 JT distortion whereas the ZnO_6 JT distortion is almost insensitive to pressure, showing values of around 0.34 Å (*C*2/*m* and *C*2). The σ_{JT} for the VO_6 octahedra in the *C*2/*c* monoclinic phase is reduced by 20% from 0.451 at ambient pressure to 0.356 Å at 15 GPa and an additional 14% reduction to 0.296 Å at 30 GPa, in contrast to the ZnO_6 polyhedra, which show a very low σ_{JT}.

For the *Pbcn* orthorhombic phase, the value of VO_6 σ_{JT} in the same pressure interval is reduced by 20%, lower than in the monoclinic structure. This result can be associated with the smaller compressibility of the *V-O6* bond (see Table 2), its values being 0.484 Å at ambient pressure and 0.384 Å at 30 GPa. Orthorhombic ZnO_6 σ_{JT} also decreases with pressure, its values varying from 0.224 Å at ambient pressure and 0.202 Å at 5 GPa to 0.153 Å at 30 GPa.

The trigonal *P*321 phase has six equal Zn-O distances, and its corresponding σ_{JT} is zero, while the two different (3+3) V-O distances lead to a VO_6 σ_{JT} of 0.464 Å at ambient pressure and 0.343 Å at 30 GPa.

The results reported in Table 2 show that the two different ZnO_6 σ_{JT} of the $P\bar{1}$ structure present an opposite behavior, the more regular one presents very low σ_{JT}, which increases by 78% up to 30 GPa, while in the more distorted ZnO_6 σ_{JT} decreases by 79%, having a value of 0.026 Å at 30 GPa. Conversely, the VO_6-1 and VO_6-2 polyhedra show a reduction of σ_{JT} of 24% and 20% in the overall range of pressures studied.

3.3 Energetics

The total energy for the studied phases, its variation relative to the *C*2/*m* structure as a reference, and the volume per formula unit calculated at the B3LYP level are presented in Table 3. The enthalpy variation relative to the *C*2/*m* structure, as a reference at the B3LYP level, ΔH, as a function of pressure for the *C*2/*m*, *C*2, *C*2/*c*, *Pbcn*, *P*321, and $P\bar{1}$ structures, as well as that of the sum of V_2O_5 and ZnO oxides, are depicted in Figure 2.

Insert Table 3 and Figure 2

An analysis of the results from Figure 2 shows that the $\Delta H - P$ curves of the *C*2/*m* and *C*2 monoclinic structures are very close to each other; therefore, both monoclinic structures may coexist in the range of pressures studied. B3LYP results indicate a pressure-induced transition between the monoclinic and the orthorhombic *Pbcn* structure at 5.0 GPa, and also show that above 15 GPa the *C*2/*c* phase becomes more stable than the other two monoclinic *C*2/*m* and *C*2 structures. The enthalpy of columbite Pbcn structure presents a sharp relative stabilization with respect to the brannerite C2/m due to sudden volume decreases. In contrast, the HSE06 and PBE functionals reveal that the orthorhombic phase has the lowest enthalpy in the pressure range from 0 to 30 GPa, whereas *C*2/*c* presents lower enthalpy than the other two monoclinic structures (above 13 GPa and 8 GPa, respectively). The trigonal *P*321 always has the highest enthalpy of all the polymorphs studied, and that of the triclinic $P\bar{1}$ is always slightly superior to that of the *C*2/*m* structure.

A note of caution is mandatory here. DFT is the most renowned computational approach to study and characterize solids[68-70] but for its success it relies on the availability of good approximations to the unknown exchange-correlation energy functional. However, it is well known that the choice of an accurate parameterization of the ground state local density approximation to this functional plays a decisive role in the ensuing rise in DFT.[71] In particular, the exchange-correlation functional as well as the fraction of exact exchange in various hybrid functionals alter the phase stability of oxide systems, [72-79] as occurs in the present study, in which the relative energies between the monoclinic and orthorhombic polymorphs as a function of an external pressure are very dependent on the functionals employed. However, the optimized geometries and values of the calculated vibrational frequencies obtained by using the three functionals are similar.

To calculate the energetics for the processes of ZnV_2O_6 decomposition into their constituent binary oxides, metals, and oxygen, V_2O_5, VO_2, ZnO, V and Zn structures have been optimized from ambient pressure up to 30 GPa. Table 4 reports the calculated values for the variations in enthalpy, $\Delta_d H^0$ at ambient pressure and temperature for the dissociation channels that were investigated. An analysis of the results shows that all channels have positive $\Delta_d H^0$ values, and the decomposition

channel $Zn\,V_2O_6 \rightarrow\ V_2O_5 + ZnO$ presents the lowest value (0.72 eV) of all the decomposition channels investigated. Therefore, for this process we studied the stability of ZnV_2O_6 against the binary oxides V_2O_5 and ZnO at different pressures.

Insert Figure 3 and Table 4

Figure 3 shows that the sum of the volumes of the ZnO and V_2O_5 is always greater than the *C2/m* ZnV_2O_6 structure with a ΔV value of 14.82 Å^3 at ambient pressure. On the other hand, the volumes of the *Pbcn* structure are lower than those of the monoclinic structure for all pressures, the decrease in the corresponding volume at 5 GPa being 5.7%. At 15 GPa there is a decrease in volume of 4.2% from the *C*2/*m* to *C*2/*c* structure.

3.4 Vibrational properties

Lattice vibrations and their behavior under pressure provide useful information regarding structural instabilities and phase transformations. Group theoretical considerations lead to the following vibrational representation at the Γ point for the *C*2/*m* structure in the standard notation:

$$\Gamma = 8A_g(\text{Raman active}) + 4B_g(\text{Raman active}) + 4A_u(\text{IR active}) + 8B_u(\text{IR active})$$

to which the acoustic modes $(A_u + 2B_u)$ should be added.[80]

As described above, the frequency calculations are performed without taking into account the anharmonicity effects. This fact and the well-known over-estimation in the frequency values obtained with the B3LYP method can explain the discrepancy with the experimental values. The calculated values for the frequencies of the Raman-active modes were corrected by a scaling factor of 0.92; the intensities as well as the Grüneisen parameters, $\gamma = \left[{}^{B_0}/_{\omega_0}\right] {}^{d\omega}/_{dP}$ have been calculated with the B_0 value reported in Table 2, and the corresponding values are listed in Table 5 together with the available experimental data. The frequencies of Raman-active modes for the *C2*, *C*2/*c*, *Pbcn*, *P*321, and $P\bar{1}$ polymorphs have also been calculated (see Tables S3-S7) in the Supporting Information).

Insert Table 5

The analysis of the Raman-active modes in Table 5 shows that the *C*2/*m* phase presents one soft mode, i.e., B_g at 288.97 cm^{-1} at ambient pressure. This mode is characterized by a decrease in the vibrational frequency with pressure (negative parameter γ). This feature suggests that at higher pressure a monoclinic brannerite-type structure should undergo a transition involving a strong coupling between a zone-centre optic mode and a strain of B_g symmetry. The *C*2 phase also shows a soft mode with negative γ, i.e., *B* at 288.51 cm^{-1}, and in addition a second mode, *A* at 308.61 cm^{-1}, with negative

γ. The *C*2/*c* structure present along a B_g rotational mode with a negative frequency with a value of -58.16 cm^{-1} at ambient pressure, -65.72 cm^{-1} at 5 GPa, -70.86 cm^{-1} at 15 GPa, -37.46 cm^{-1} at 20 GPa, and -62.71 cm^{-1} at 30 GPa shows the existence of a slight dynamical instability across all the range of studied pressures. For the C2/c monoclinic structure we calculated the elastic properties at pressures from ambient to 30 GPa and the Born criteria was applied being this monoclinic structure always mechanical stable. The 13 corresponding elastic coefficients (in GPa) of the elastic tensor at ambient pressure and at 15 GPa are shown in Table S8 of the Supporting Information, that follows the criteria for mechanical stability. The *P*321 trigonal phase presents one rotational *E* soft mode at ambient pressure with a frequency of 53.64 cm^{-1}, with a Grüneisen parameter of -10.82. This mode has a negative frequency above 15 GPa. In the case of the remaining orthogonal *Pbcn* and the triclinic $P\bar{1}$ structures, all the frequencies increase on raising the pressure.

We employed Badger's rule [81] to analyze the presence of electron charge processes along with the compression of different polymorphs. This rule states that the strength of a bond correlates with the frequency (ω) of its vibrational mode, $\omega = A/(r_{MO} - B)^{3/2}$, where A and B are constants and r_{MO} is the metal−oxygen distance. If this rule is followed by the breathing vibrational modes of the ZnO_6 and VO_6 polyhedra, we can state that the behavior of the frequencies with pressure is due only to geometrical factors, while if the rule is not fulfilled, charge transfer or other factors are involved. Badger's rule is fulfilled for the *Pbcn*, *P*321, and $P\bar{1}$ polymorphs, indicating that the variation in the structure of these three polymorphs with pressure has a geometrical origin. In contrast, for the monoclinic *C*2/*m*, *C*2, and *C*2/*c* polymorphs, Badger's rule is not followed by two A_g breathing modes (854.11 and 989.02 cm^{-1}) in the case of *C*2/*m*, by two breathing modes *A* (855.29 cm^{-1}) and *B* (912.74 cm^{-1}) in the case of *C*2, and by one A_g breathing mode (869.91 cm^{-1}) in the case of *C*2/*c*. In addition, as shown in Figure 4 for the *C*2/*m*-ZnV_2O_6 structure and in Figures S2 and S3 in the supporting material for the *C*2 and *C*2/*c* polymorphs, there is a trend shift around 5 GPa in the plot of $\omega^{3/2}$ versus (1/d). The stabilization of the monoclinic structures is mainly due to electronic factors (see the next section).

Insert Figure 4

3.5 Electronic properties

Figure 5 shows the calculated B3LYP bulk band structure along the adequate symmetry lines of the Bravais lattices and the total DOS and that projected on atoms, for the ZnV_2O_6 polymorphs studied.

Insert Figure 5

The transition is indirect in monoclinic, orthorhombic, trigonal, and triclinic band structures. For the *C*2/*m* and *C*2 phases, the valence band (VB) maximum and the conduction band (CB) minimum are located at L (½,0,½) and V (0,0,½) *k*-points, respectively. Contrary to the case of the other two monoclinic structures, for the *C*2/*c* polymorph, the VB maximum is located near Γ (0,0,0), whereas the bottom of the CB is at the *k*-point (0,0,⅓) near V (0,0,½). For the *Pbcn* lattice, the VB maximum is located at Γ (0,0,0) and the bottom of the CB is in the vicinity of the Y (0,¼,0) *k*-point for the *P*321 polymorph, at Γ (0,0,0) and L (½,0,½) *k*-points, respectively, whereas in the case of the triclinic $P\bar{1}$ polymorph, they are at Y (½,0,0) and A (½,½,0) and k-points, respectively. For the *C*2/*m* and the other two monoclinic structures, calculations predict that the top of the VB is composed mostly of O *2p* orbitals, while at the bottom of the CB the contribution of V $3d_{yz}$, and $3d_{xy}$ orbitals predominate over $3d_z^2$ and $3d_{xz}$ orbitals, and Zn *4s*. In the case of the remaining *Pbcn*, *P*321, and $P\bar{1}$ structures, the top of the VB is also mostly due to the O *2p* orbitals, while the bottom of the CB consists predominantly of V $3d_z^2$, $3d_{yz}$ and $3\,d_{x^2-y^2}$ orbitals. Therefore these states will dominate the behavior of the band gap as observed in other vanadates.[82,83]}

Insert Figure 6

The band gaps (E_g) are 3.87, 3.88, 3.83, 3.63, 3.27, and 3.90 eV for the *C*2/*m*, *C*2, *C*2/*c*, *Pbcn*, *P*321, and $P\bar{1}$ polymorphs, respectively. The effect of pressure on the band structures of the studied polymorphs has also been examined in the present study. Under compression, the O states move toward higher energies faster than the V states, thereby producing a small reduction in E_g. The hydrostatic band-gap deformation potential,[84] a_g, can be defined as the product of the bulk modulus and the variation of E_g with pressure $a_g = B_0\, {dE_g}/{dP}$. Figure 6 shows the pressure dependence of the indirect E_g for the monoclinic *C*2/*m*, *C*2, *C*2/*c*, orthorhombic *Pbcn*, trigonal *P*321, and triclinic $P\bar{1}$ ZnV_2O_6 structures up to 30 GPa. As commented above, all polymorphs have an indirect band gap. An analysis of the results shows that the band gap of the *C2/m* and *C*2 phases decreases with pressure from 3.88 to 3.62 eV, while for *C*2/*c* it decreases from 3.83 to 3.33 eV, the *Pbcn* phase being less sensitive to pressure. Conversely, the *P*321 structure shows the lowest E_g values, from 3.27 at ambient pressure to 3.10 eV at 30 GPa, and for the triclinic $P\bar{1}$ E_g decreases from 3.90 to 3.59 eV, their a_g values being: -1.27, -1,19, -2.59 ,+0.06, -0.85 and -1.28 eV, respectively.

In order to evaluate the influence of the electronic factors on the pressure behavior of the different structures, we calculated the Mulliken atomic charges, focusing mainly on the monoclinic *C*2/*m*, *C*2, and *C*2/*c* phases with the aim of explaining why Badger's rule is not fulfilled in these polymorphs. The choice of the Mulliken partition is arbitrary because there is no single method of

performing the partition of the charge density. However, the choice of the given scheme remains extremely useful when comparing the results of calculations performed using similar basis sets.[85]

Due to the small changes in the values of the Mulliken atomic charges, it is more convenient to plot the relative changes of the sum of the values for the atomic charges of the ZnO_6 and VO_6 units with respect to the value of zero pressure. In Figure 7 the relative variation of the sum of the Mulliken charges of the ZnO_6 and VO_6 polyhedra from ambient up to 30 GPa is presented for the *C*2/*m* monoclinic polymorph (for *C*2 and *C*2/*c*, see Figures S4 and S5 in the supporting information). An analysis of the results shows that a charge transfer takes place from the ZnO_6 to the VO_6 units when an external pressure is applied, this transfer being of 0.061 e^- at 30 GPa (0.024 e^- for the *C*2 structure at 20 GPa, and 0.098 e^- for the *C*2/*c* structure at 30 GPa). This behavior can explain why Badger's rule is not fulfilled by the monoclinic-ZnV_2O_6.

4 Conclusions

The properties of solids as a function of pressure are of fundamental interest to a wide range of areas in condensed matter physics and chemistry. High pressure could alter the properties of materials and chemical bonds, giving rise to some novel structures (polymorphs) and exhibiting phenomena, and physical and chemical properties that are not accessible under ambient conditions. Pressure-induced phase transitions are a critical phenomenon, which describes the interplay between the intermolecular and intramolecular distances. However, from the experimental side, high pressure is not easy to achieve/access and control in X-ray diffraction experiments in a diamond anvil cell. In this context, the utilization and application of reliable theoretical methods and techniques are widely acknowledged ways of obtaining the properties and behavior of materials under high pressure.

An understanding of the origins and atomistic mechanisms of the structural transformations is essential to improve the performance of existing materials and for a rational design of new ones with even better characteristics. For this purpose, in this work, a systematic investigation has been performed using first-principle calculations, at the DFT level, on the stability, geometry, and electronic properties of the six stable ZnV_2O_6 phases found. The objective of the present paper was to explore, analyze, and find metastable polymorphs of ZnV_2O_6 that can be accessible through high-pressure synthesis. As the energetic separation and the structural differences between the polymorphs are small and thus potentially sensitive to details of the computational procedure, we have placed special

emphasis on the influence of different approximations for the exchange-correlation functional (B3LYP, HSE06, and PBE).

On the basis of our calculations, the behavior of this compound under pressure can be rationalized in terms of both local polyhedral, and the corresponding structural changes can be associated to Zn-O and V-O bond distances of ZnO_6 octahedra and VO_6 octahedra, and the relative compressibility of $Zn-O$ and $V-O$ bonds of each polymorph.

Our findings can be summarized as follows:

1) From the twelve polymorphs studied, ten thermodynamically stable structures have been successfully identified as stationary points in the potential energy hypersurface at ambient pressure, while only five of them are minima in the range of 0-30 GPa, i.e., *C*2, *C2/m*, *Pbcn*, *P*321, $P\bar{1}$ phases; additionally, the *C*2/*c* structure displays one very low imaginary frequency in the range of ambient up to GPa, and is also considered as a possible stable polymorph**.** The *Pnma*, *C*222, $P4_2/mmm$, and $P\bar{3}1m$ polymorphs present structural instabilities as shown by the presence of several imaginary frequencies between -400 and -100 cm^{-1} over the entire range of pressures studied. The optimization of ZnV_2O_6 within the $I\bar{4}2m$ and *Pbca* space groups has been unsuccessful.

2) *C2/m* and *C2* monoclinic structures show very close $\Delta H - P$ curves and they coexist in the range of 0-30 GPa. In both cases, V cations show a distorted octahedral coordination with oxygen ions, the V-O5 distance being very sensitive to pressure.

3) Calculated values derived from the enthalpy-pressure representation show that the monoclinic structure (*C2/m* or *C2*) transforms to the *Pbcn* orthorhombic structure at 5.0 GPa at the B3LYP level. On the other hand, the *C*2/*c* polymorph becomes more stable than the other two monoclinic (*C2/m* and *C2*) structures at 15 GPa. However, the calculations performed by using the HSE06 and PBE functionals show that the *C*2/*c* becomes the most stable of the monoclinic structures above 13 and 8 GPa, respectively, and that the orthorhombic structure is the most stable polymorph in the range 0-30 GPa, and. These results indicate that the relative energies between the monoclinic and orthorhombic polymorphs as a function of an external pressure are very dependent on the functionals that are employed; however, the optimized geometries and values of the calculated vibrational frequencies obtained by using the three functionals are similar**.**

4) Badger's rule is fulfilled for the *Pbcn*, *P*321, and $P\bar{1}$ polymorphs, indicating that the variation of the structure with pressure has a geometrical origin. In contrast, the monoclinic *C*2/m and *C*2 structures each present two breathing modes and *C*2/*c* has one mode that do not follow Badger's rule due to a charge transfer from the ZnO_6 to the VO_6 polyhedra.

5) An analysis of the results shows that all channels have positive $\Delta_d H^0$ values and so the decomposition channels are not energetically feasible.

6) Monoclinic (*C2/m*, C2, *C*2/*c*), orthorhombic (*Pbcn*), trigonal (*P*321), and triclinic ($P\bar{1}$) phases present semiconductor behavior with large indirect band gaps. The band gap of the *C2/m*, C2, *C*2/*c*, and $P\bar{1}$ phases decreases with pressure, their diminution from 0 to 30 GPa being 6.7, 6.7, 13.0, and 8.0%, respectively, whereas that of the *Pbcn* structure is less sensitive to pressure and rises slightly on increasing the pressure. The trigonal *P*321 structure presents the lowest band gaps, which decrease by 5.3% with pressure, from P=0 to 30 GPa.

The present work provides insight into fundamental scientific issues and the current results will pave the way for further experimental exploration of the presence of metastable polymorphs of ZnV_2O_6 materials. We expect that these encouraging results will stimulate the material science community to transform our *in silico* proposed ZnV_2O_6 polymorphs into the real world, e.g. by obtaining ZnV_2O_6-based materials using high-pressure synthesis.

Supporting Information

The Supporting Information is available free of charge on the ACS Publications website. Structural data, calculated frequencies (Raman intensities and Grüneisen parameters), elastic coefficients.

Acknowledgments

The authors acknowledge Universitat Jaume I for project UJI-B2016-25, Generalitat Valenciana for project *PrometeoII*/2014/022, ACOMP/2014/270, and ACOMP/2015/1202, and Ministerio de Economia y Competitividad (Spain) project CTQ2015-65207-P for supporting this research financially. This work was also supported by the Spanish MALTA-Consolider Ingenio 2010 Program (Project CSD2007-00045). The authors are grateful to Prof. Roberto Orlando (Crystal2014) for his help on some aspects of the final version of the manuscript.

References

(1) Hemley, R. J.; Ashcroft, N. W. The Revealing Role Of Pressure in the Condensed Matter Sciences. *Physics Today* **1998**, *51*, 26.

(2) Hemley, R. J. Effects Of High Pressure On Molecules. *Annual Review of Physical Chemistry* **2000**, *51*, 763.

(3) Grochala, W.; Hoffmann, R.; Feng, J.; Ashcroft, N. W. The Chemical Imagination at Work in Very Tight Places. *Angewandte Chemie-International Edition* **2007**, *46*, 3620.

(4) Isaak, D. G. Ultrahigh-pressure mineralogy: physics and chemistry of the Earth's deep interior. In *Reviews in Mineralogy*; (Ed.), R. J. H., Ed.; Mineralogical Society of America: Washington, DC, 1998; Vol. 37, p p. 671.

(5) Ballaran, T. B.; Kurnosov, A.; Trots, D. Single-crystal X-ray diffraction at extreme conditions: a review. *High Pressure Research* **2013**, *33*, 453.

(6) Lee, R.; Howard, J. A. K.; Probert, M. R.; Steed, J. W. Structure of organic solids at low temperature and high pressure. *Chemical Society Reviews* **2014**, *43*, 4300.

(7) Machon, D.; Meersman, F.; Wilding, M. C.; Wilson, M.; McMillan, P. F. Pressure-induced amorphization and polyamorphism: Inorganic and biochemical systems. *Progress in Materials Science* **2014**, *61*, 216.

(8) Manaa, M. R.; Fried, L. E. The Reactivity of Energetic Materials Under High Pressure and Temperature. In *Advances in Quantum Chemistry, Vol 69*; Sabin, J. R., Ed. 2014; Vol. 69, p 221.

(9) Bhardwaj, P.; Singh, S. Pressure induced structural phase transitions-A review. *Central European Journal of Chemistry* **2012**, *10*, 1391.

(10) Goncharov, A. F.; Howie, R. T.; Gregoryanz, E. Hydrogen at extreme pressures. *Low Temperature Physics* **2013**, *39*, 402.

(11) Klug, D. D.; Yao, Y. Metallization of solid hydrogen: the challenge and possible solutions. *Physical Chemistry Chemical Physics* **2011**, *13*, 16999.

(12) McMahon, M. I.; Nelmes, R. J. High-pressure structures and phase transformations in elemental metals. *Chemical Society Reviews* **2006**, *35*, 1341.

(13) Zurek, E.; Grochala, W. Predicting crystal structures and properties of matter under extreme conditions via quantum mechanics: the pressure is on. *Physical Chemistry Chemical Physics* **2015**, *17*, 2917.

(14) Dubrovinsky, L.; Dubrovinskaia, N. Comprehensive Inorganic Chemistry II. Elsevier: 2013; Vol. 2, p 223.

(15) *An Introduction to High-Pressure Science and Technology*; CRC Press: Boca Raton, 2015.

(16) Boldyreva, E. V. *Anisotropic Compression. What can it Teach us About Intermolecular Interactions? in High-Pressure Crystallography. From Novel Experimental Approaches to Applications in Cutting-Edge Technologies*; Springer: Dordrecht, 2010

(17) Wang, Y.; Ma, Y. Perspective: Crystal structure prediction at high pressures. *The Journal of Chemical Physics* **2014**, *140*, 040901.

(18) Zhang, L. J.; Wang, Y. C.; Lv, J.; Ma, Y. M. Materials discovery at high pressures. *Nature Reviews Materials* **2017**, *2*.

(19) Liu, G.; Kong, L. P.; Gong, J.; Yang, W. G.; Mao, H. K.; Hu, Q. Y.; Liu, Z. X.; Schaller, R. D.; Zhang, D. Z.; Xu, T. Pressure-Induced Bandgap Optimization in Lead-Based Perovskites with Prolonged Carrier Lifetime and Ambient Retainability. *Advanced Functional Materials* **2017**, *27*.

(20) Umeyama, D.; Lin, Y.; Karunadasa, H. I. Red-to-Black Piezochromism in a Compressible Pb-l-SCN Layered Perovskite. *Chemistry of Materials* **2016**, *28*, 3241.

(21) Zhu, J. L.; Quan, Z. W.; Lin, Y. S.; Jiang, Y. B.; Wang, Z. W.; Zhang, J. Z.; Jin, C. Q.; Zhao, Y. S.; Liu, Z. X.; Brinker, C. J.; Xu, H. W. Porous Ice Phases with VI and Distorted VII Structures Constrained in Nanoporous Silica. *Nano Letters* **2014**, *14*, 6554.

(22) Jayaraman, A. Diamond Anvil Cell and High-Pressure Physical Investigations. *Reviews of Modern Physics* **1983**, *55*, 65.

(23) Wackerle, J. Shock-Wave Compression of Quartz. *Journal of Applied Physics* **1962**, *33*, 922.

(24) Zhang, L.; Wang, Y.; Lv, J.; Ma, Y. Materials discovery at high pressures. *Nature Reviews Materials* **2017**, *2*.

(25) Gracia, L.; Beltran, A.; Andres, J. A Theoretical Study on the Pressure-Induced Phase Transitions in the Inverse Spinel Structure Zn2SnO4. *Journal of Physical Chemistry C* **2011**, *115*, 7740.

(26) Gracia, L.; Beltran, A.; Errandonea, D.; Andres, J. CaSO4 and Its Pressure-Induced Phase Transitions. A Density Functional Theory Study. *Inorganic Chemistry* **2012**, *51*, 1751.

(27) Beltran, A.; Gracia, L.; Longo, E.; Andres, J. First-Principles Study of Pressure-Induced Phase Transitions and Electronic Properties of Ag2MoO4. *Journal of Physical Chemistry C* **2014**, *118*, 3724.

(28) Beltran, A.; Gracia, L.; Andres, J.; Longo, E. First-Principles Study on Polymorphs of AgVO3: Assessing to Structural Stabilities and Pressure-Induced Transitions. *Journal of Physical Chemistry C* **2017**, *121*, 27624.

(29) McCrone, W. C. *Physics and chemistry of the organic solid state*; Wiley Interscience: New York, USA, 1965; Vol. 2.

(30) Gondrand, M.; Collomb, A.; Joubert, J. C.; Shannon, R. D. Synthesis of New High-Pressure Columbite Phases Containing Pentavalent Vanadium. *Journal of Solid State Chemistry* **1974**, *11*, 1.

(31) Mocala, K.; Ziolkowski, J. Polymorphism of the Bivalent-Metal Vanadates MgV2O6, CaV2O6, MnV2O6, CoV2O6, NiV2O6, CuV2O6, ZnV2O6, CdV2O6. *Journal of Solid State Chemistry* **1987**, *69*, 299.

(32) Beck, H. P. The co-ordination number rule and the rule of hardness, powerful tools to rationalize inorganic structures. *Zeitschrift Fur Kristallographie-Crystalline Materials* **2014**, *229*, 473.

(33) Stefanidis, T.; Nord, A. G.; Kierkegaard, P. The Crystal-Structure of Calcium Metaasenate, CaAs2O6. *Zeitschrift Fur Kristallographie* **1985**, *173*, 313.

(34) Tealdi, C.; Mozzati, M. C.; Malavasi, L.; Ciabattoni, T.; Amantea, R.; Azzoni, C. B. Columbite-type FexMn1-xNb2O6 solid solution: structural and magnetic characterization. *Physical Chemistry Chemical Physics* **2004**, *6*, 4056.

(35) Bouloux, J. C.; Perez, G.; Galy, G. Crystal-Structure of Metavanadates CaV2O6 and CdV2O6 Alpha - Polymorphic Alpha-Beta Transformation. *Bulletin De La Societe Francaise Mineralogie Et De Cristallographie* **1972**, *95*, 130.

(36) Karpov, O. G.; Simonov, M. A.; Krasnenko, T. I.; Zabara, O. A. Crystal-Structure of Alpha-SrV2O6. *Kristallografiya* **1989**, *34*, 1392.

(37) Yao, T.; Oka, Y.; Yamamoto, N. Structure Refinement of Barium Metavanadate BaV2O6. *Inorganica Chimica Acta* **1995**, *238*, 165.

(38) Angenault, J.; Rimsky, A. Crystalline Structure of Phase HgV206 Obtained at High Temperature. *Comptes Rendus Hebdomadaires Des Seances De L Academie Des Sciences Serie C* **1968**, *266*, 978.

(39) Müller Buschbaum, H.; Kobel, M. Ein neuer Strukturtyp der Oxovanadate MV2O6: NiV2O6. *Z. Anorg. Allg. Chem.* **1991**, *596*, 23.

(40) Sillen, L. G.; Lundborg, K. La2MoO6, a lanthanum oxy-molybdate with a layer structure. *Zeitschrift Fur Anorganische Und Allgemeine Chemie* **1943**, *252*, 2.

(41) Loye, O.; Laruelle, P.; Harari, A. Crystalline Structure of Form of Low Temperature of Double Oxide ThTi206. *Comptes Rendus Hebdomadaires Des Seances De L Academie Des Sciences Serie C* **1968**, *266*, 454.

(42) Mitchell, R. H.; Chakhmouradian, A. R. Solid solubility in the system NaLREETi2O6-ThTi2O6 (LREE, light rare-earth elements): experimental and analytical data. *Physics and Chemistry of Minerals* **1999**, *26*, 396.

(43) Butt, F. K.; Idrees, F.; Tahir, M.; Cao, C.; Hussain, R.; Ahmed, R.; Haq, B. U. Fabrication of ZnV2O6 nanostructures: Their energy storage and PL properties. *Materials Letters* **2015**, *155* 15.

(44) Andreetti, G. D.; Calestani, G.; Montenero, A.; Bettinelli, M. Refinement of the Crystal-Structure of ZnV2O6. *Zeitschrift Fur Kristallographie* **1984**, *168*, 53.

(45) Tang, R.; Li, Y.; Li, N.; Han, D.; Li, H.; Zhao, Y.; Gao, C.; Zhu, P.; Wang, X. Reversible Structural Phase Transition in ZnV2O6 at High Pressures. *Journal of Physical Chemistry C* **2014**, *118*, 10560.

(46) Dovesi, R.; Saunders, V. R.; Roetti, C.; Orlando, R.; Zicovich-Wilson, C. M.; Pascale, F.; Civalleri, B.; Doll, K.; Harrison, N. M.; Bush, I. J.; D'Arco, P.; Llunell, M.; Causà, M.; Noël, Y. CRYSTAL14 User's Manual (University of Torino, Torino 2014).

(47) Becke, A. D. Density-Functional Thermochemistry. The Role of Exact Exchange. *Journal of Chemical Physics* **1993**, *98*, 5648.

(48) Lee, C. T.; Yang, W. T.; Parr, R. G. Development of the Colle-Salvetti Correlation-Energy Formula into a Functional of the Electron-Density. *Physical Review B* **1988**, *37*, 785.

(49) Heyd, J.; Scuseria, G. E.; Ernzerhof, M. Hybrid functionals based on a screened Coulomb potential. *Journal of Chemical Physics* **2006**, *124*.

(50) Perdew, J. P.; Wang, Y. Accurate and Simple Analytic Representation of the Electron-Gas Correlation-Energy. *Physical Review B* **1992**, *45*, 13244.

(51) http://www.crystal.unito.it/Basis_Sets/Ptable.html.

(52) Grimme, S. Semiempirical GGA-type density functional constructed with a long-range dispersion correction. *Journal of Computational Chemistry* **2006**, *27*, 1787.

(53) Bucko, T.; Hafner, J.; Lebegue, S.; Angyan, J. G. Improved Description of the Structure of Molecular and Layered Crystals: Ab Initio DFT Calculations with van der Waals Corrections. *Journal of Physical Chemistry A* **2010**, *114*, 11814.

(54) Maschio, L.; Kirtman, B.; Rerat, M.; Orlando, R.; Dovesi, R. Ab initio analytical Raman intensities for periodic systems through a coupled perturbed Hartree-Fock/Kohn-Sham method in an atomic orbital basis. II. Validation and comparison with experiments. *J. Chem. Phys.* **2013**, *139*, 161101.

(55) Broyden, C. G. The convergence of a class of double-rank minimization algorithms I: General considerations. *J. Inst. Math. Appl.* **1970**, *6*, 76.

(56) Broyden, C. G. The convergence of a class of double-rank minimization algorithms I: General considerations. *J. Inst. Math. Appl.* **1970**, *6*, 222.

(57) Fletcher, R. A New Approach to Variable Metric Algorithms. *Comput. J.* **1970**, *13*, 317.

(58) Goldfarb, D. A Family of Variable Metric Updates Derived by Variational Means. *Math. Comput.* **1970**, *24*, 23.

(59) Shanno, D. F. Conditioning of quasi-Newton methods for function minimization. *Math. Comput.* **1970** *24*, 647.

(60) Melissen, S. T. A. G.; Labat, F.; Sautet, P.; Bahers, T. L. Electronic properties of PbX3CH3NH3 (X = Cl, Br, I) compounds for photovoltaic and photocatalytic applications. *Physical Chemistry Chemical Physics* **2015**, *17*, 2199.

(61) Wu, Z.-j.; Zhao, E.-j.; Xiang, H.-p.; Hao, X.-f.; Liu, X.-j.; Meng, J. *Physical Review B* **2007**, *76*, 054115.

(62) Birch, F. Elasticity and Constitution of the Earth Interior. *Journal of Geophysical Research* **1952**, *57*, 227.

(63) Bocharov, D.; Gryaznov, D.; Zhukovskii, Y. F.; Kotomin, E. A. Ab initio Modeling of Oxygen Impurity Atom Incorporation into Uranium Mononitride Surface and Sub-Surface Vacancies. *Journal of Nuclear Materials* **2011**, *416*, 200.

(64) Dorado, B.; Freyss, M.; Martin, G. GGA plus U Study of the Incorporation of Iodine in Uranium Dioxide. *European Physical Journal B* **2009**, *69*, 203.

(65) Lee, Y. L.; Kleis, J.; Rossmeisl, J.; Morgan, D. Ab initio Energetics of LaBO3(001) (B=Mn, Fe, Co, and Ni) for Solid Oxide Fuel Cell Cathodes. *Physical Review B* **2009**, *80*, 224101.

(66) Martinez, J. I.; Hansen, H. A.; Rossmeisl, J.; Norskov, J. K. Formation Energies of Rutile Metal Dioxides Using Density Functional Theory. *Physical Review B* **2009**, *79*, 045120.

(67) Ruiz-Fuertes, J.; Friedrich, A.; Pellicer-Porres, J.; Errandonea, D.; Segura, A.; Morgenroth, W.; Haussühl, E.; Tu, C.-Y.; Polian, A. Structure Solution of the High-Pressure Phase of CuWO4 andEvolution of the Jahn_Teller Distortion. *Chem. Mater.* **2011**, *23*, 4220.

(68) Kohn, W.; Sham, L. J. Self-Consistent Equations Including Exchange and Correlation Effects. *Physical Review* **1965**, *140*, 1133.

(69) Burke, K. Perspective on density functional theory. *Journal of Chemical Physics* **2012**, *136*.

(70) Jones, R. O. Density functional theory: Its origins, rise to prominence, and future. *Reviews of Modern Physics* **2015**, *87*, 897.

(71) Perdew, J. P.; Zunger, A. Self-Interaction Correction to Density-Functional Approximations for Many-Electron Systems. *Physical Review B* **1981**, *23*, 5048.

(72) Curnan, M. T.; Kitchin, J. R. Investigating the Energetic Ordering of Stable and Metastable TiO2 Polymorphs Using DFT plus U and Hybrid Functionals. *Journal of Physical Chemistry C* **2015**, *119*, 21060.

(73) Gerosa, M.; Bottani, C. E.; Caramella, L.; Onida, G.; Di Valentin, C.; Pacchioni, G. Electronic structure and phase stability of oxide semiconductors: Performance of dielectric-dependent

hybrid functional DFT, benchmarked against GW band structure calculations and experiments. *Physical Review B* **2015**, *91*.

(74) Labat, F.; Baranek, P.; Domain, C.; Minot, C.; Adamo, C. Density functional theory analysis of the structural and electronic properties of TiO2 rutile and anatase polytypes: Performances of different exchange-correlation functionals. *Journal of Chemical Physics* **2007**, *126*.

(75) Landmann, M.; Rauls, E.; Schmidt, W. G. The electronic structure and optical response of rutile, anatase and brookite TiO2. *Journal of Physics-Condensed Matter* **2012**, *24*.

(76) Muscat, J.; Swamy, V.; Harrison, N. M. First-principles calculations of the phase stability of TiO2. *Physical Review B* **2002**, *65*.

(77) Ochoa-Calle, A. J.; Zicovich-Wilson, C. M.; Hernandez-Lamoneda, R.; Ramirez-Solis, A. Understanding the epsilon and zeta High-Pressure Solid Phases of Oxygen. Systematic Periodic Density Functional Theory Studies Using Localized Atomic Basis. *Journal of Chemical Theory and Computation* **2015**, *11*, 1195.

(78) Ricca, C.; Ringuede, A.; Cassir, M.; Adamo, C.; Labat, F. A Comprehensive DFT Investigation of Bulk and Low-Index Surfaces of ZrO2 Polymorphs. *Journal of Computational Chemistry* **2015**, *36*, 9.

(79) Yu, H. Y. S.; Li, S. H. L.; Truhlar, D. G. Perspective: Kohn-Sham density functional theory descending a staircase. *Journal of Chemical Physics* **2016**, *145*.

(80) http://www.cryst.ehu.es/cgi-bin/cryst/programs//nph-sam Bilbao Crystallographic Server: IR Raman Hyper Raman modes.

(81) Badger, R. M. A Relation Between Internuclear Distances and Bond Force Constants. *Journal of Chemical Physics* **1934**, *2*.

Birch, F. *Journal of Geophysical Research* **1952**, *57*, 227.

(82) Panchal, V.; Errandonea, D.; Segura, A.; Rodriguez-Hernandez, P.; Muñoz, A.; Lopez-Moreno, S.; Bettinelli, M. *Journal of Applied Physics* **2011**, *110*, 043723.

(83) Muñoz-Santiuste J. E.; Lavín V.; Rodríguez-Mendoza U. R.; Ferrer-Roca C.; Errandonea D.; Martínez-García D.; Rodríguez-Hernández P.; Muñoz A.; Bettinelli M. *Phys. Chem. Chem. Phys.* **2018**, *20*, 27314.

(84) Schweitzer, C.; Reimann, K.; Steube, M. Two-photon spectroscopy of SnO(2) under hydrostatic pressure. *Solid State Communications* **1999**, *110*, 697.

(85) Pisani, C. D., R.; Roetti, C. *Hartree-Fock Ab Initio Treatment of Crystalline Systems*; Springer: Berlin, 1988; Vol. 48.

Table Captions

Table 1. Calculated and available experimental values of the cell parameters and bulk modulus, B_0, and its pressure derivative, B_0', for the ZnV_2O_6 geometries (a) brannerite *C*2/*m*, (b) brannerite *C*2, (c) $ThTi_2O_6$-type *C*2/*c*, (d) columbite *Pbcn*, (e) $CaAs_2O_6$-type *P*321, and (f) NiV_2O_6-type $P\bar{1}$.

Table 2. Optimized values, at the B3LYP level, of the Zn-O and V-O bond lengths and σ_{JT} parameters (in Å) of the ZnO_6 and VO_6 distorted octahedra from 0 GPa to 30 GPa, their multiplicity, and the corresponding bond compressibility, χ.

Table 3. The total energy for all the phases studied at the B3LYP level, its variation relative to the brannerite *C*2/*m* structure as a reference, and the volume per molecular unit.

Table 4. B3LYP calculated values of the decomposition enthalpy, $\Delta_d H^0$, for different dissociation channels of ZnV_2O_6 toward binary oxides (V_2O_5, ZnO and VO_2), metal (V and Zn), and oxygen.

Table 5. B3LYP calculated, corrected with a scaling factor of 0.92, and observed Raman mode frequencies of brannerite *C*2/*m*, as well as calculated intensities at ambient pressure (in arbitrary units) and Grüneisen parameters (γ).

Figure Captions

Figure 1. Polyhedral representation of the brannerite *C*2/*m* (a), brannerite *C*2 (b), $ThTi_2O_6$-type *C*2/*c* (c), columbite *Pbcn* (d), $CaAs_2O_6$-type *P*321 (e), and NiV_2O_6-type $P\bar{1}$ (f) structures.

Figure 2. B3LYP enthalpy variation values, ΔH, in (eV) as a function of pressure for brannerite *C*2/*m*, brannerite *C*2, $ThTi_2O_6$-type *C*2/*c*, columbite *Pbcn*, $CaAs_2O_6$-type *P*321 and NiV_2O_6-type $P\bar{1}$ structures, and for the binary oxides V_2O_5 and ZnO (taking the *C*2/*m* structure as a reference).

Figure 3. Calculated variation in B3LYP volume with pressure of ZnV_2O_6 phases and the binary oxides V_2O_5 and ZnO. (b) Calculated variation in B3LYP volume with pressure of ZnV_2O_6 phases.

Figure 4. Badger's plot for the two A_g (854.11 and 989.02 cm^{-1} at ambient pressure) breathing modes of the brannerite *C*2/*m* phase.

Figure 5. B3LYP band structure and total DOS and projected DOS on atoms for brannerite *C*2/*m* (a), $ThTi_2O_6$-type (b), columbite (c), $CaAs_2O_6$-type (d), and NiV_2O_6-type (e) ZnV_2O_6 polymorphs.

Figure 6. Evolution of E_g with pressure for brannerite *C*2/*m*, brannerite *C*2, $ThTi_2O_6$-type *C*2/*c*, columbite *Pbcn*, $CaAs_2O_6$-type *P*321 and NiV_2O_6-type $P\bar{1}$ ZnV_2O_6 structures, calculated at the B3LYP level.

Figure 7. Variation of the sum of the Mulliken atomic charges of the ZnO_6 and VO_6 polyhedra versus pressure for the brannerite *C*2/*m* ZnV_2O_6 structure.

Table 1.

(a) *C*2/*m*

	B3LYP	HSE06	PBE	Ref. 44	Ref. 43	Ref. 45
a (Å)	9.242	9.166	9.234	9.265	9.245	9.245
b (Å)	3.528	3.505	3.547	3.524	3.528	3.533
c (Å)	6.573	6.439	6.521	6.589	6.576	6.579
β (º)	111.13	112.99	112.57	111.37		111.7
V_0 (Å^3)	199.908	186.602	197.219			
B_0 (GPa)	146.74	152.18	147.39			147
B_0'	5.11	5.54	5.09			4 fixed

(b) *C*2

	B3LYP	HSE06	PBE	Ref. 38	Ref. 45
a (Å)	9.240	9.167	9.234	9.242	
b (Å)	3.529	3.505	3.548	3.526	
c (Å)	6.574	6.439	6.521	6.574	
β (º)	111.05	113.00	112.59	111.55	
V_0 (Å^3)	200.033	190.419	197.207		
B_0 (GPa)	137.25	152.35	147.51		137
B_0'	6.24	5.53	5.08		4 fixed

(c) ***C2/c***

	B3LYP	HSE06	PBE
a (Å)	10.064	9.979	10.027
b (Å)	8.356	8.290	8.362
c (Å)	4.955	4.902	4.931
β (º)	118.50	118.54	118.63
V_0 (Å^3)	366.216	356.210	362.860
B_0 (GPa)	151.38	160.09	149.27
B_0'	4.96	4.96	4.86

(d) *Pbcn*

	B3LYP	HSE06	PBE	Ref. 30
a (Å)	13.483	13.389	13.644	13.579
b (Å)	5.548	5.488	5.604	5.589
c (Å)	4.793	4.757	4.812	4.824
V_0 (Å^3)	358.572	349.515	357.565	
B_0 (GPa)	163.73	210.27	166.15	
B_0'	5.50	4.73	5.03	

(e) *P*321

	B3LYP	HSE06	PBE
a (Å)	4.693	4.646	4.684
c (Å)	4.907	4.864	4.886
V_0 (Å^3)	93.589	90.929	92.853
B_0 (GPa)	147.77	157.89	147.88
B_0'	5.40	5.41	5.33

(f) $\boldsymbol{P\bar{1}}$

	B3LYP	HSE06	PBE
a (Å)	4.753	4.711	4.744
b (Å)	7.105	7.044	7.079
c (Å)	8.808	8.727	8.770
α (º)	102.17	102.18	102.14
β (º)	90.23	90.27	90.19
γ (º)	94.24	94.40	94.86
V_0 (Å^3)	289.920	282.159	286.824
B_0 (GPa)	122.82	128.72	124.10
B_0'	5.74	5.45	5.29

Table 2.

Zn-O/V-O distances (Å)	0 GPa	5 GPa	15 GPa	30 GPa	Multiplicity	χ (10^{-3} GPa^{-1})
*C*2/*m*						
Zn-O1	1.950	1.928	1.892	1.854	2	1.64
Zn-O2	2.217	2.199	2.167	2.125	4	1.40
$\sigma_{JT(Zn)}$	0.334	0.339	0.343	0.338		
V-O1	1.662	1.660	1.655	1.649	1	0.25
V-O1'	1.681	1.682	1.678	1.669	1	0.25
V-O2'	1.844	1.833	1.816	1.794	2	0.90
V-O3'	2.102	2.093	2.077	2.054	1	0.77
V-O4'	2.447	2.353	2.247	2.162	1	3.88
$\sigma_{JT (V)}$	0.667	0.597	0.522	0.467		
*C*2						
Zn-O1	1.950	1.928	1.892	1.854	2	1.64
Zn-O2'	2.217	2.198	2.167	2.125	4	1.40
$\sigma_{JT (Zn)}$	0.309	0.314	0.318	0.313		
V-O1	1.662	1.660	1.655	1.649	1	0.26
V-O1'	1.681	1.682	1.678	1.669	1	0.25
V-O2'	1.844	1.833	1.816	1.794	2	0.90
V-O3'	2.102	2.093	2.076	2.053	1	0.78
V-O4'	2.446	2.353	2.247	2.163	1	3.86
$\sigma_{JT (V)}$	0.667	0.597	0.522	0.467		
C2/c						
Zn-O1	2.072	2.047	2.025	1.976	2	1.77
Zn-O2	2.101	2.075	2.031	1.996	2	1.89
Zn-O3	2.113	2.082	2.036	2.000	2	2.01
$\sigma_{JT (Zn)}$	0.041	0.036	0.031	0.025		
V-O1'	1.702	1.705	1.707	1.710	1	-0.17
V-O1	1.723	1.721	1.718	1.715	1	0.16
V-O2'	1.749	1.746	1.741	1.737	1	0.26

V-O3	2.035	2.015	1.984	1.956	2	1.51
V-O4'	2.172	2.128	2.065	2.016	1	2.71
$\sigma_{JT\ (V)}$	0.451	0.413	0.359	0.296		
Pbcn						
Zn-O1	1.995	1.976	1.944	1.906	2	1.49
Zn-O2	2.065	2.050	2.023	1.987	2	1.26
Zn-O3	2.214	2.176	2.118	2.059	2	2.34
$\sigma_{JT\ (Zn)}$	0.224	0.202	0.175	0.153		
V-O3	1.663	1.659	1.651	1.640	1	0.46
V-O1	1.755	1.754	1.751	1.743	1	0.22
V-O1'	1.763	1.760	1.755	1.746	1	0.31
V-O2'	2.010	1.994	1.962	1.925	1	1.41
V-O4'	2.051	2.032	1.999	1.961	1	1.47
V-O5'	2.223	2.195	2.151	2.102	1	1.82
$\sigma_{JT\ (V)}$	0.484	0.461	0.423	0.384		
*P*321						
Zn-O1	2.143	2.112	2.066	2.014	6	2.01
V-O1	1.721	1.719	1.715	1.708	3	0.27
V-O1'	2.100	2.072	2.031	1.988	3	1.80
$\sigma_{JT\ (V)}$	0.464	0.432	0.387	0.343		
$P\bar{1}$						
Zn1-O1	2.031	2.010	1.977	1.945	2	1.41
Zn1-O2	2.034	2.011	1.981	1.950	2	1.37
Zn1-O3	2.052	2.040	2.015	1.981	2	1.12
$\sigma_{JT\ (Zn)}$	0.023	0.034	0.042	0.041		
Zn2-O1	2.015	1.999	1.972	1.941	2	1.23
Zn2-O2	2.036	2.020	1.992	1.957	2	1.29
Zn2-O3	2.040	2.023	1.993	1.959	2	1.34
Zn2-O4	2.049	2.027	1.994	1.961	2	1.44
Zn2-O5	2.089	2.060	2.018	1.961	2	2.05
Zn2-O6	2.167	2.098	2.024	1.978	2	2.91
$\sigma_{JT\ (Zn)}$	0.123	0.079	0.043	0.026		

V1-O3	1.608	1.611	1.611	1.607	1	0.02
V1-O4	1.704	1.697	1.689	1.681	1	0.44
V1-O5	1.876	1.864	1.846	1.824	1	0.93
V1-O6	1.983	1.977	1.962	1.941	1	0.70
V1-O7	2.098	2.085	2.054	2.012	1	1.36
V1-O8	2.353	2.287	2.220	2.157	1	2.77
$\sigma_{JT\,(V)}$	0.606	0.560	0.511	0.463		
V2-O1	1.616	1.615	1.612	1.607	1	0.18
V2-O2	1.703	1.698	1.690	1.683	1	0.39
V2-O5	1.859	1.850	1.835	1.816	1	0.77
V2-O6	1.989	1.981	1.966	1.947	1	0.71
V2-O7	2.110	2.096	2.062	2.014	1	1.48
V2-O8	2.315	2.262	2.208	2.157	1	2.27
$\sigma_{JT\,(V)}$	0.583	0.547	0.506	0.466		
V3-O1	1.666	1.669	1.6573	1.643	1	0.46
V3-O2	1.676	1.670	1.6697	1.668	1	0.17
V3-O3	1.778	1.768	1.7555	1.743	1	0.65
V3-O4	1.779	1.769	1.758	1.746	1	0.62

Table 3.

Phase	E/ZnV_2O_6 (arb. units)	ΔE (eV)	V/ZnV_2O_6 ($Å^3$)
*C*2/*m*	-4118.712588	0.000	99.954
*C*2	-4118.712585	$8 \cdot 10^{-5}$	100.016
*C*2/c	-4118.698727	0.377	91.554
Pbcn	-4118.711334	0.034	89.643
Pnma	-4118.681592	0.843	93.858
*C*222	-4118.658351	1.475	113.233
$P4_2/mmm$	-4118.667094	1.237	88.360
$P\bar{3}1m$	-4118.680377	0.876	89.009
*P*321	-4118.611619	2.746	93.589
$P\bar{1}$	-4118.709097	0.094	96.640

Table 4.

Dissociation channel	$\Delta_d H^0$(eV)
$Zn\,V_2O_6 \rightarrow\ V_2O_5 + ZnO$	0.72
$Zn\,V_2O_6 \rightarrow\ V_2O_5 + Zn + \frac{1}{2}O_2$	2.59
$Zn\,V_2O_6 \rightarrow\ 2VO_2 + \frac{1}{2}O_2 + ZnO$	3.22
$Zn\,V_2O_6 \rightarrow\ 2V + Zn + 3O_2$	18.89

Table 5.

Raman Mode	ω (cm^{-1})	ω (cm^{-1})*0.92	Intensity (arb. units)[$]	γ	Ref. 45	Assignment[#]
B_g	170.09	156.48	0.00	0.60	143	$\nu(VO_2)^b + \nu(OV_2)^b$
A_g	177.11	162.94	22.29	1.31	168	$\nu(VO_2)^b$
A_g	245.24	225.62	32.81	1.00	218	$\nu(VO_2)^b$
B_g	288.97	265.85	0.00	-0.13	267	$\nu(OZnOVO)^b$
B_g	328.69	302.39	0.00	0.64	300	$\nu(VO_2)^b$
A_g	329.97	303.57	127.32	0.34		$\nu(VO_2)^b + \nu(VO_2)^b$
A_g	387.66	356.65	98.37	0.63	348	$\nu(VO_2)^b$
A_g	491.05	451.77	1000.00	0.64	431	$\nu(VO_2)^b$
A_g	555.42	510.99	57.36	0.42	514	$\nu(VO_2)^b + \nu(OV_2)^b$
B_g	744.71	685.13	0.00	0.69	716	$\nu(VO)^{str}$
A_g	854.11	785.78	13.00	0.38	784	$\nu(VO)^{str}$
A_g	989.02	909.90	17.81	0.28	914	$\nu(VO)^{str}$

[$] Intensities do not take into account temperature or frequency of the incoming laser and are normalized to the highest peak, arbitrarily set to 1000.00.

[#] str, stretching; *b*, bending

Figures

Figure 1.

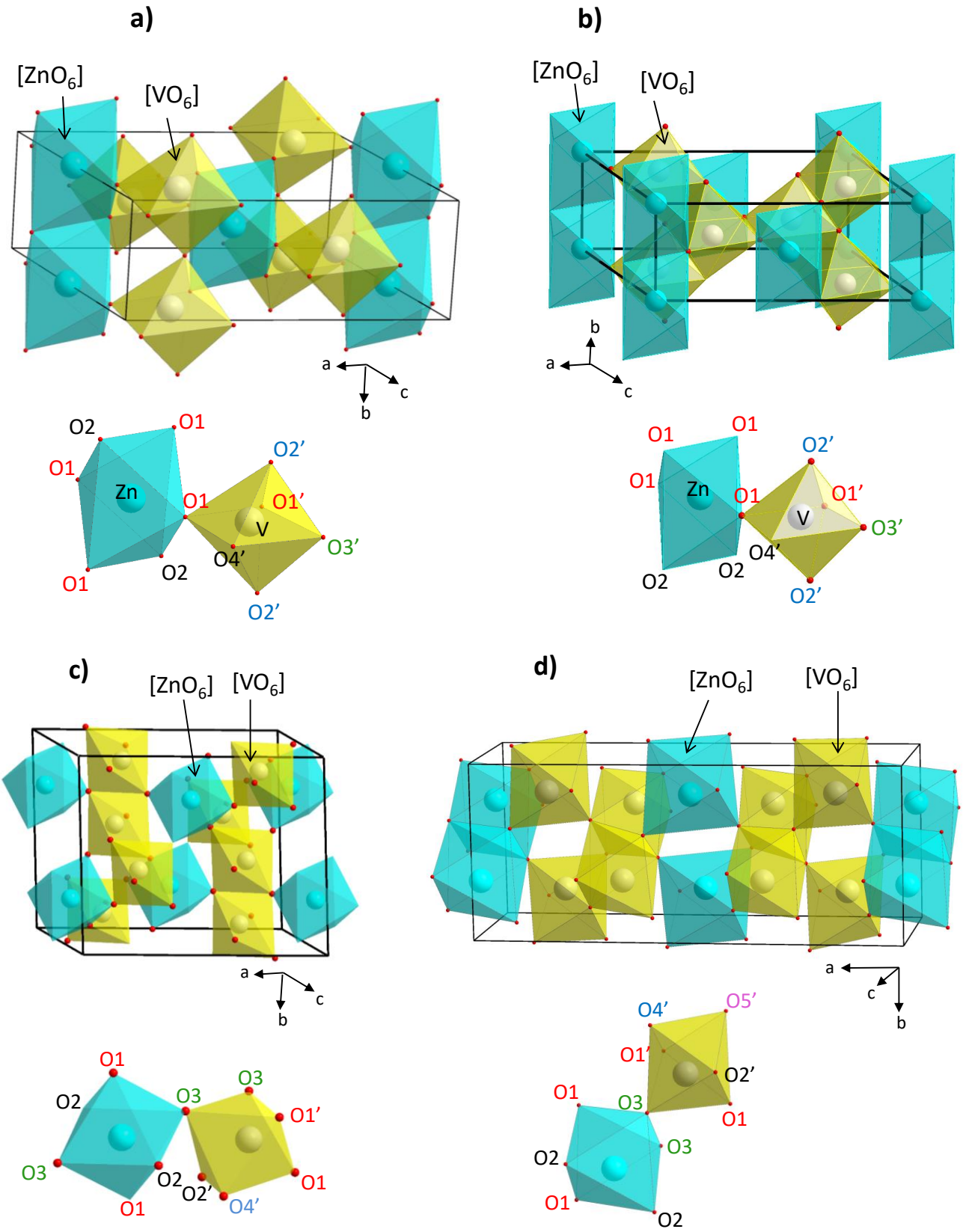

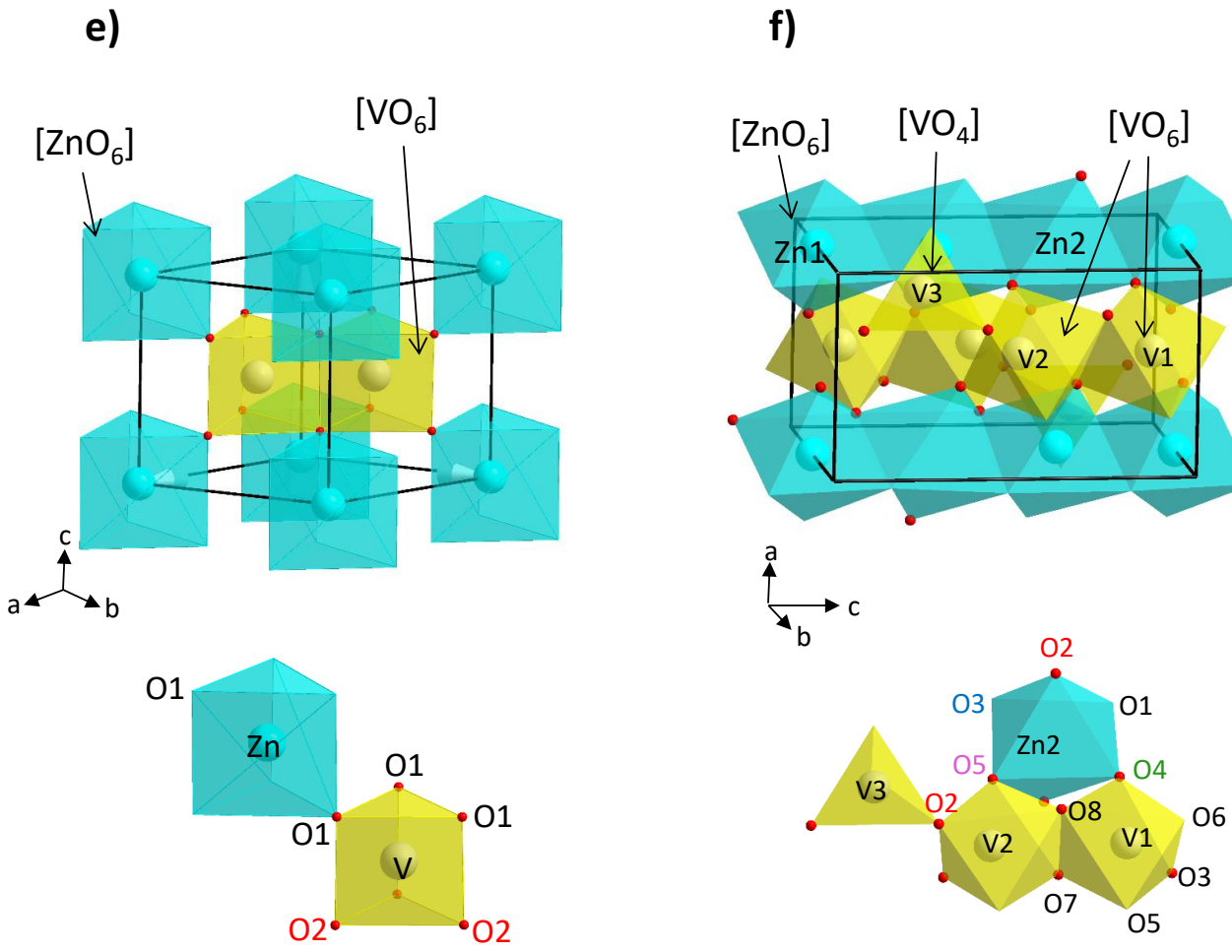
e)
[ZnO6]
[VO6]
c
a
b
O1
Zn
O1
O1
O1
V
O2
O2
f)
[ZnO6]
[VO4]
[VO6]
Zn1
V3
Zn2
V2
V1
a
c
b
O2
O3
O1
Zn2
O5
O4
V3
O2
O8
O6
V2
V1
O3
O7
O5

Figure 2

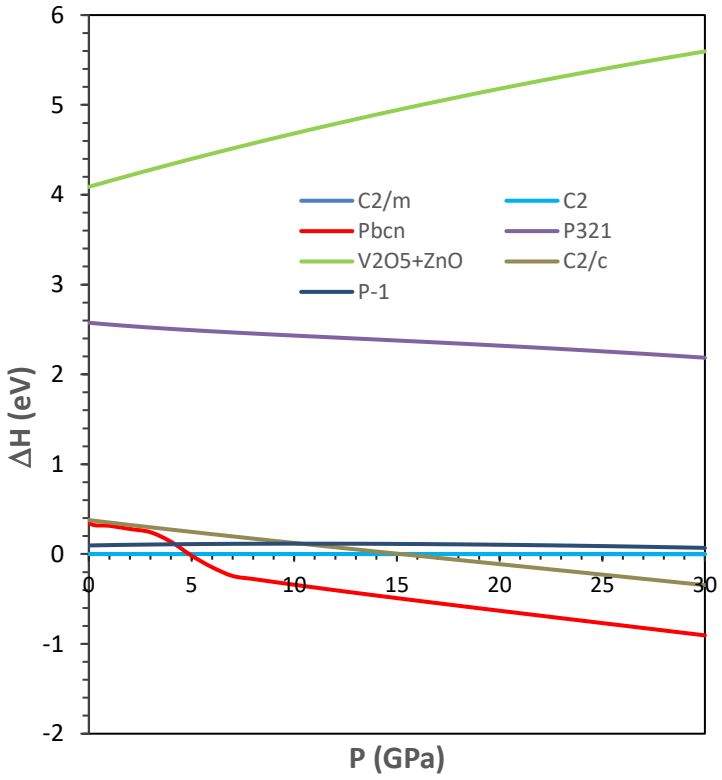

Figure 3

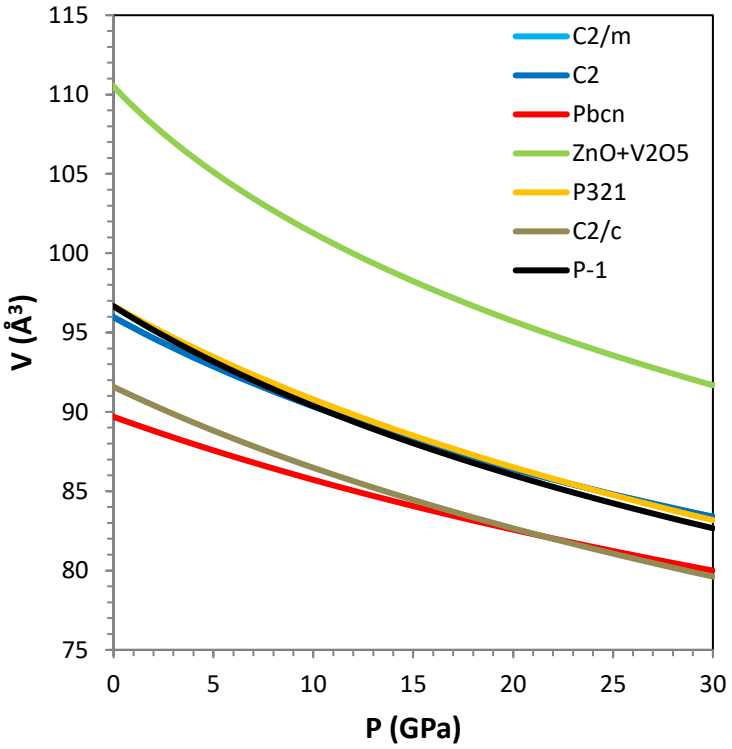

Figure 4

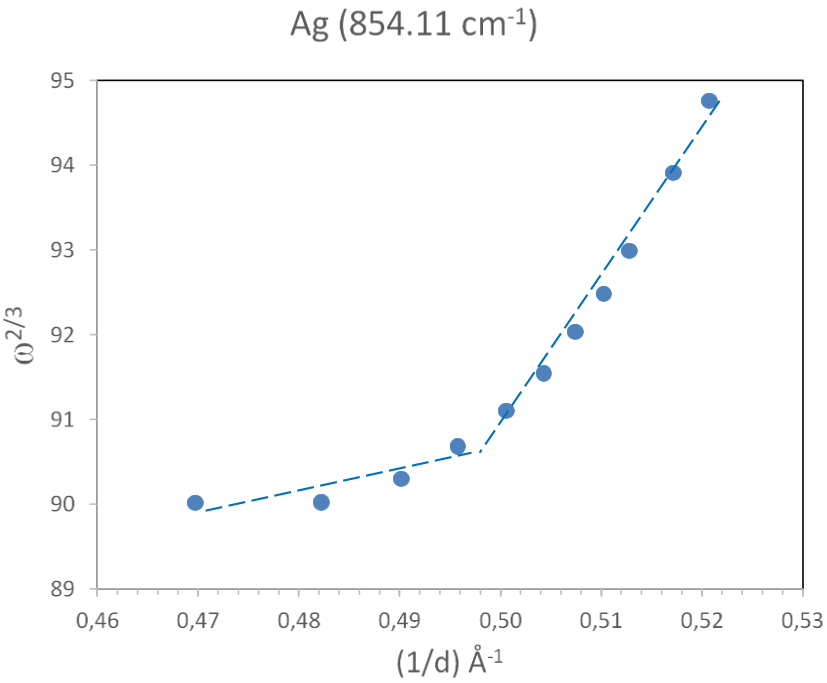
Ag (854.11 cm-1)
95
94
93
92
91
90
89
ω2/3
0,46
0,47
0,48
0,49
0,50
0,51
0,52
0,53
(1/d) Å-1

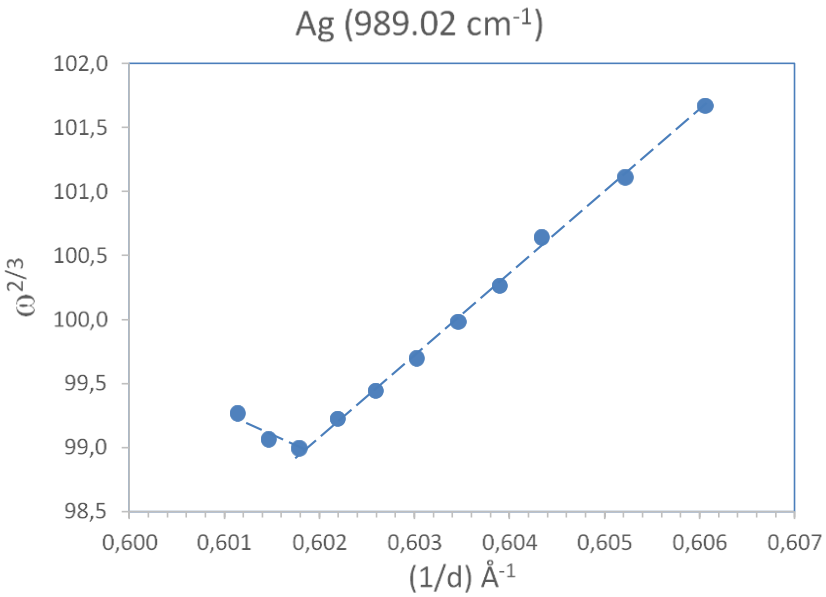
Ag (989.02 cm-1)
102,0
101,5
101,0
100,5
100,0
99,5
99,0
98,5
ω2/3
0,600
0,601
0,602
0,603
0,604
0,605
0,606
0,607
(1/d) Å-1

Figure 5

(a)

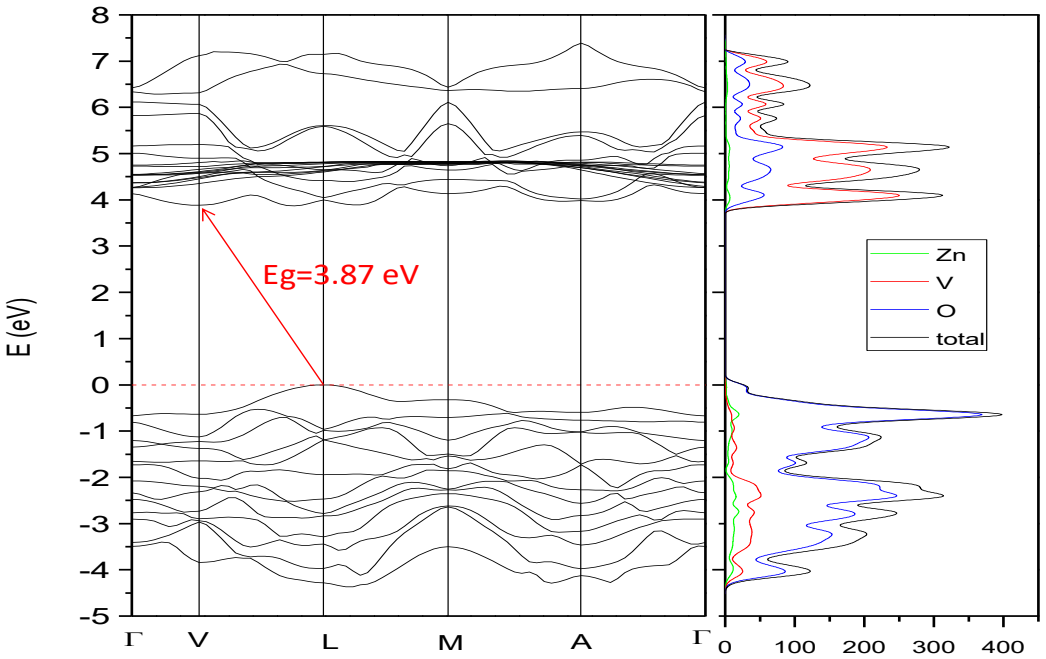
Eg=3.87 eV
E (eV)
Γ
V
L
M
A
Γ
Zn
V
O
total
0
100
200
300
400

(b)

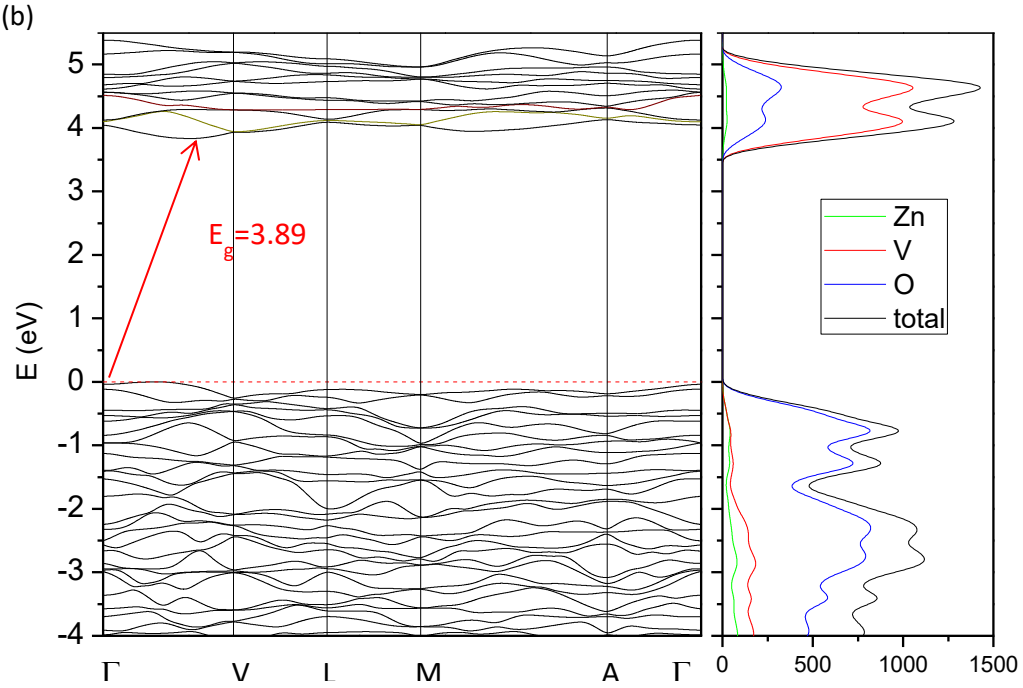
E_g=3.89
E (eV)
Γ
V
L
M
A
Γ
Zn
V
O
total
0
500
1000
1500

(c)

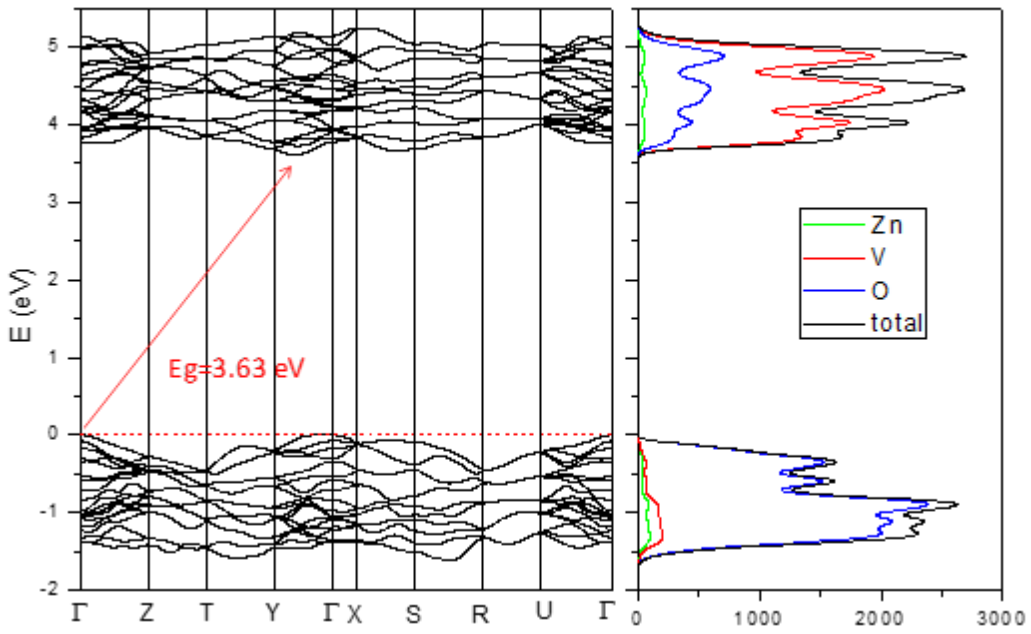
E (eV)
Eg=3.63 eV
Γ Z T Y Γ X S R U Γ
Zn
V
O
total
0 1000 2000 3000

(d)

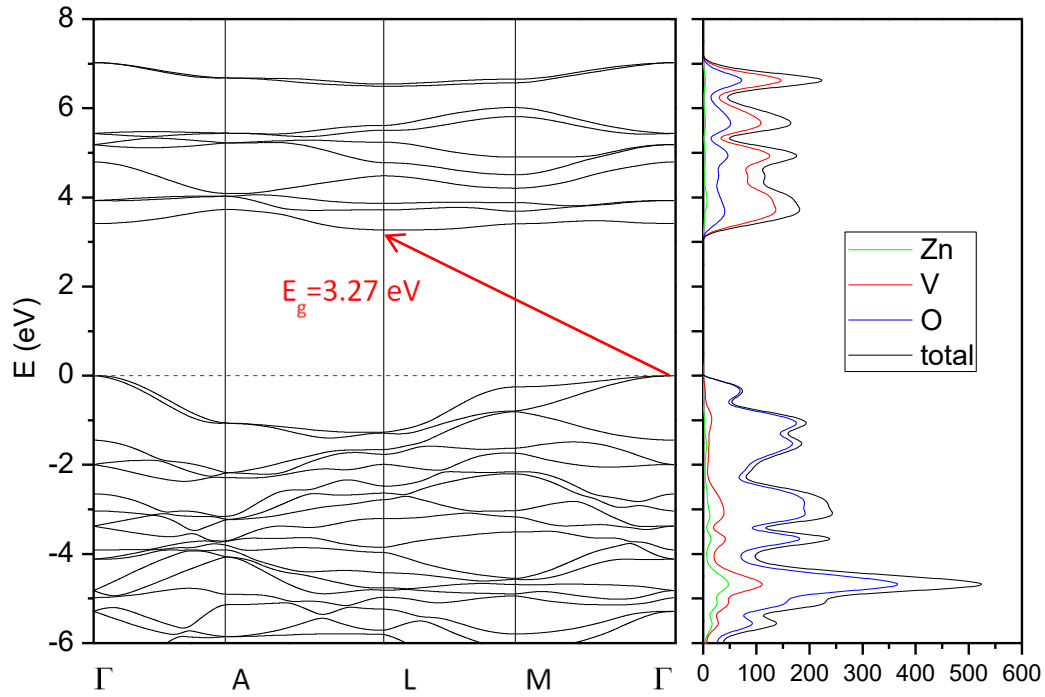
E (eV)
E g =3.27 eV
Γ A L M Γ
Zn
V
O
total
0 100 200 300 400 500 600

(e)

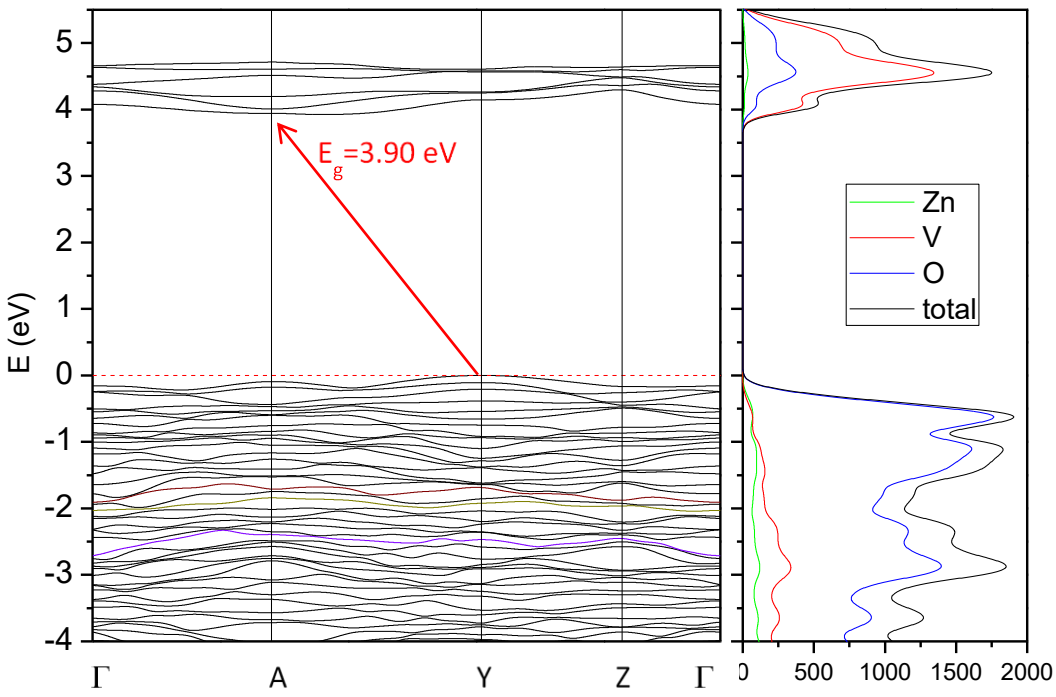
E (eV)
5
4
3
2
1
0
-1
-2
-3
-4
Γ
A
Y
Z
Γ
E_g =3.90 eV
Zn
V
O
total
0
500
1000
1500
2000

Figure 6

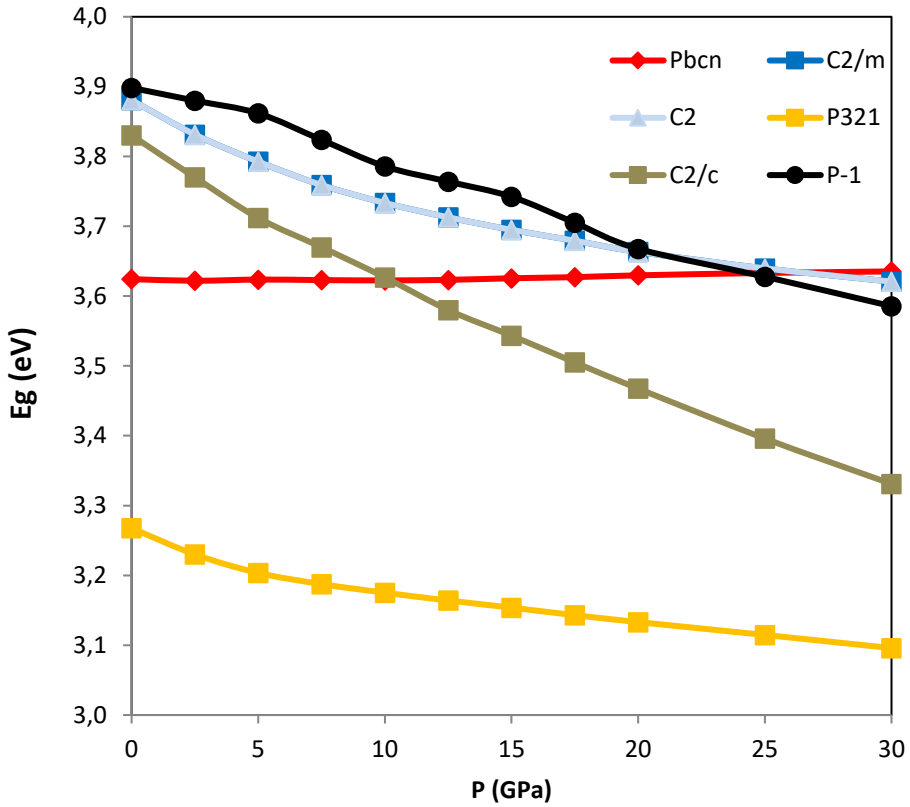

Figure 7